MOX-Report No. 50/2025

Conforming and discontinuous discretizations of non-isothermal Darcy–Forchheimer flows

Bonetti, S.; Botti, M.; Antonietti, P.F.

MOX, Dipartimento di Matematica
Politecnico di Milano, Via Bonardi 9 - 20133 Milano (Italy)

mox-dmat@polimi.it https://mox.polimi.it

Conforming and discontinuous discretizations of non-isothermal Darcy–Forchheimer flows

Stefano Bonetti[1], Michele Botti[1], and Paola F. Antonietti[1]

[1] *MOX-Dipartimento di Matematica, Politecnico di Milano, Piazza Leonardo da Vinci 32, Milan, 20133, Italy*

Abstract

We present and analyze in a unified setting two schemes for the numerical discretization of a Darcy-Forchheimer fluid flow model coupled with an advection-diffusion equation modeling the temperature distribution in the fluid. The first approach is based on fully discontinuous Galerkin discretization spaces. In contrast, in the second approach, the velocity is approximated in the Raviart-Thomas space, and the pressure and temperature are still piecewise discontinuous. A fixed-point linearization strategy, naturally inducing an iterative splitting solution, is proposed for treating the nonlinearities of the problem. We present a unified stability analysis and prove the convergence of the iterative algorithm under mild requirements on the problem data. A wide set of two- and three-dimensional simulations is presented to assess the error decay and demonstrate the practical performance of the proposed approaches in physically sound test cases.

Keywords: Darcy-Forchheimer, heat equation, discontinuous Galerkin, Raviart-Thomas, polytopal methods, geophysics.

MSC: 65N12, 65N30, 74F05, 76S05.

1 Introduction

This research addresses the numerical modeling of temperature distribution in fluids governed by the Darcy–Forchheimer (DF) law, which relates the fluid velocity vector to the pressure gradient and is applicable in regimes where the fluid velocity is sufficiently high. In such cases, the classical Darcy law—where the velocity is linearly proportional to the pressure gradient—fails to capture the underlying physics accurately. Previous studies [25, 31] have demonstrated that Darcy's law provides reliable predictions primarily for low velocities and low-porosity media. However, nonlinear effects become significant whenever high flow velocities and/or variable porosity are involved, leading to the need for an additional quadratic velocity term. The DF law incorporates both the Darcy term and the nonlinear inertial term, the latter scaling with the square of the fluid velocity and arising from inertial forces. Moreover, in relevant geophysical processes such as geothermal energy extraction and greenhouse gas sequestration, thermal effects, modeled via an advection–diffusion equation, are also particularly relevant since temperature variations strongly influence fluid properties. The resulting model is therefore fully coupled: the velocity field governs thermal advection, while temperature variations affect fluid density and viscosity, thereby altering the flow field. Moreover, it is nonlinear due to (i) the temperature-dependent viscosity, (ii) the quadratic Forchheimer term, and (iii) the nonlinear advection term in the temperature equation.

Extensive research has been conducted on the Forchheimer equation, starting from experimental investigations [39]. The mathematical analysis of the DF model has been considered in [36]. Concerning the numerical discretization, we refer, e.g., to [33, 35, 38] for mixed finite element discretizations. Regarding the coupling of flow models with the heat equation, we refer, e.g., to [15, 16], where a

comprehensive analysis of the Darcy model coupled with the heat equation is presented. Heat convection in a liquid medium whose motion is described by the Stokes/Navier Stokes equations has been extensively studied; among others, we mentioned the papers [1, 2, 9, 26, 28]. Recently, there has been a growing interest in the study of a coupled DF-heat model. In [3, 27, 37] the authors propose an approximation based on standard finite elements (with the introduction of *bubble* functions for treating the velocity field). Moreover, in [3] a singular source term for the heat equation is considered. In [30] the problem is approximated via a block-centered finite difference scheme.

In this work, we study the coupled Darcy–Forchheimer–heat model and present and analyze two numerical discretization schemes for its numerical discretization. The first scheme (referred to as dG-dG-dG) employs an entirely discontinuous finite element formulation for the velocity, pressure, and temperature fields. The second scheme (referred to as RT-dG-dG) adopts a conforming Raviart–Thomas finite element space for the velocity, combined with discontinuous approximations for the pressure and temperature fields. The difference between the two approaches lies in the choice of the discretization space for the velocity field, that is, discontinuous Galerkin [13] for the first case and Raviart-Thomas [32, 34] for the second one. The two approaches offer complementary advantages. The dG–dG–dG scheme is remarkably versatile, as it supports polytopal meshes (see [4, 14, 22] for dG schemes on polytopal meshes). We remark that polytopal methods are particularly advantageous in computational geoscience due to their geometric flexibility in the process of mesh design, efficient handling of highly heterogeneous media, as well as natural support of domain-specific features (e.g., fractures) without prohibitive computational costs. In the context of geophysics, PolyDG methods have been applied to flows in fracture porous media [5], poroelasticity [6], and thermo-hydro-mechanical models [10, 18]. For heat-type problems discretized using PolyDG methods, we refer, e.g., [23]. We refer to [24] for a comprehensive monograph on PolyDG methods, and to [7] for a review of the current development of PolyDG methods for geophysical applications.

In this work, we propose a robust treatment of the convection term, following the thermo-poroelasticity framework in [19], with the key distinction that here the temperature field is advected by the fluid velocity rather than the Darcy velocity. The corresponding nonlinearities are addressed via an iterative linearization algorithm, which naturally leads to a splitting-based solution strategy. The main contributions of the proposed numerical framework are: *(a)* a detailed formulation of the dG–dG–dG and RT–dG–dG schemes, emphasizing the treatment of the nonlinear advection term and the corresponding linearization strategy; *(b)* a unified analysis establishing stability of the discrete problem and convergence of the fixed-point iteration; and *(c)* an extensive set of two- and three-dimensional numerical experiments demonstrating convergence properties and validating the method in established benchmarks.

The rest of the paper is organized as follows: the model problem and its weak formulation are presented in Section 2. In Section 3, we present the two discretization schemes together with the corresponding linearization strategy. In Section 4, we prove, in a unified setting, the stability of the discrete problem and the convergence of the fixed-point linearization algorithm. Two- and three-dimensional numerical results assessing the convergence properties and benchmark test cases are shown discussed in Section 5.

2 Model problem

Let $\Omega \subset \mathbb{R}^d$, with $d \in \{2; 3\}$, be an open bounded Lipschitz domain. The non-isothermal DF problem reads: *find* $(\mathbf{u}, p, T)$ *such that in* Ω *it holds:*

$$\nu(T)\mathbf{K}^{-1}\,\mathbf{u} + \beta|\mathbf{u}|\mathbf{u} + \nabla p = \mathbf{f}, \tag{1a}$$

$$\nabla\cdot\mathbf{u} = 0, \tag{1b}$$

$$-\nabla\cdot(\boldsymbol{\Theta}\nabla T) + (\mathbf{u}\cdot\nabla)\,T = g, \tag{1c}$$

where $|\cdot|$ denotes the Euclidean vector norm, namely $|\mathbf{u}|^2 = \mathbf{u}^T\,\mathbf{u}$. In (1), the variables $(\mathbf{u}, p, T)$ represent the velocity, the pressure, and the temperature, respectively. The function $\mathbf{f} : \Omega \to \mathbb{R}^d$ represents an external body force, while $g : \Omega \to \mathbb{R}$ is the heat source. Equations (1a), (1b), and

(1c) represent the DF fluid flow, the incompressibility of the fluid, and the heat transfer, respectively. The description of the DF flow is characterized by the Forchheimer coefficient β that represents the strength of the inertial effects in the porous medium: it is the ratio between the pressure drop caused by fluid–solid interactions and the one caused by viscous and inertia resistances. If β were null, then (1a) would reduce to the Darcy equation. We observe that the couplings between (1a) and (1c) are bi-directional. Namely, we observe that the temperature T influences the kinematic viscosity of the fluid $\nu(\cdot)$; moreover, in the heat transfer equation we have the presence of a convective term of the form $(\mathbf{u}\cdot\nabla)\,T$, hence the fluid flow affects the temperature field. The kinematic viscosity $\nu(\cdot):\mathbb{R}\to\mathbb{R}^+$ is a bounded $\mathcal{C}^1(\mathbb{R}^+)$, globally Lipschitz function. For the numerical investigation, we consider a particular model function $\nu(S)=1+e^{-S}$ [27].

Symbol	Unit	Quantity	Symbol	Unit	Quantity
ν	Pa s	fluid viscosity	β	$\mathrm{Pa\,s^2/m^3}$	Forchheimer coefficient
$\mathbf{K}$	$\mathrm{m^2}$	permeability	$\boldsymbol{\Theta}$	$\mathrm{m^2/s}$	thermal conductivity

Table 1: Model parameters appearing in (1)

In Table 1 we detail the parameters characterizing problem (1) specifying their physical interpretation and unit of measure. To close problem (1), different types of boundary conditions can be considered (e.g. Dirichlet, Robin, or Neumann). If a full Neumann condition on the velocity is imposed, then the mean value of the pressure must be prescribed. For the sake of simplicity, in the rest of the article, we consider homogeneous Dirichlet conditions for both the pressure and temperature fields.

2.1 Weak formulation

In this section, we present the weak formulation of problem (1). To this aim, we first introduce some notation and assumptions.

For $X\subseteq\Omega$, we denote by $L^p(X)$ the standard Lebesgue space of index $p\in[1,\infty]$ and by $H^q(X)$ the Sobolev space of index $q\geq 0$ of real-valued functions defined on X, with the convention that $H^0(X)=L^2(X)$. The notation $\mathbf{L}^p(X)$ and $\mathbf{H}^q(X)$ is adopted in place of $[L^p(X)]^d$ and $[H^q(X)]^d$, respectively. In addition, we denote by $\mathbf{H}(\mathrm{div},X)$ the space of $\mathbf{L}^2(X)$ vector fields whose divergence is square integrable. These spaces are equipped with natural inner products and norms denoted by $(\cdot,\cdot)_X=(\cdot,\cdot)_{L^2(X)}$ and $||\cdot||_X=||\cdot||_{L^2(X)}$, respectively, with the convention that the subscript can be omitted in the case $X=\Omega$. For the sake of brevity, we make use of the symbol $x\lesssim y$ to denote $x\leq Cy$, where C is a positive constant independent of the discretization parameters. We also introduce the following assumptions on the problem data.

Assumption 2.1 (Regularity assumptions on the problem data)**.** We assume that the problem data satisfy the following regularity conditions.

1. The permeability $\mathbf{K}=(K)_{i,j=1}^d$ and thermal conductivity $\boldsymbol{\Theta}=(\Theta)_{i,j=1}^d$ are symmetric tensor fields which, for strictly positive real numbers $k_M>k_m$ and $\theta_M>\theta_m$, satisfy for a.e. $x\in\Omega$:
$$k_m|\zeta|^2\leq\zeta^T\mathbf{K}(x)\zeta\leq k_M|\zeta|^2\quad\text{and}\quad\theta_m|\zeta|^2\leq\zeta^T\boldsymbol{\Theta}(x)\zeta\leq\theta_M|\zeta|^2\quad\forall\zeta\in\mathbb{R}^d.$$
2. The fluid viscosity ν and the Forchheimer coefficient β are scalar fields such that $\nu:\Omega\to[\nu_m,\nu_M]$ and $\beta:\Omega\to[0,\beta_M]$ with $0<\nu_m\leq\nu_M$ and $0\leq\beta_M$.
3. The forcing terms satisfy $\mathbf{f}\in\mathbf{L}^2(\Omega)$ and $g\in L^2(\Omega)$.

We can now introduce the weak formulation of problem (1). Let $\mathbf{Z}=\{\mathbf{z}\in\mathbf{L}^3(\Omega):\nabla\cdot\mathbf{z}\in L^2(\Omega)\}$, $W=L^2(\Omega)$, $W=L^2(\Omega)$, and $V=H_0^1(\Omega)$, the weak formulation formulation reads: *find* $(\mathbf{u},p,T)\in\mathbf{Z}\times W\times V$ *such that:*

$$\begin{aligned}&\mathcal{M}_\nu(T,\mathbf{u},\mathbf{v})+\mathcal{M}_\beta(\mathbf{u},\mathbf{u},\mathbf{v})-(p,\nabla\cdot\mathbf{v})+(q,\nabla\cdot\mathbf{u})\\&+(\boldsymbol{\Theta}\nabla T,\nabla S)+((\mathbf{u}\cdot\nabla)\,T,S)=(\mathbf{f},\mathbf{v})+(g,S)\qquad\forall(\mathbf{v},q,S)\in\mathbf{Z}\times W\times V,\end{aligned}\tag{2}$$

where the trilinear forms $\mathcal{M}_\nu : V \times \mathbf{Z} \times \mathbf{Z} \to \mathbb{R}$ and $\mathcal{M}_\beta : \mathbf{Z} \times \mathbf{Z} \times \mathbf{Z} \to \mathbb{R}$ are given by

$$\mathcal{M}_\nu(T, \mathbf{u}, \mathbf{v}) = (\nu(T)\mathbf{K}^{-1}\,\mathbf{u}, \mathbf{v}), \quad \mathcal{M}_\beta(\mathbf{w}, \mathbf{u}, \mathbf{v}) = (\beta|\mathbf{w}|\mathbf{u}, \mathbf{v}).$$

Remark 2.1. *The choice of the Banach space* $\mathbf{Z}$ *follows from the derivation of the weak formulation. Indeed, applying the Hölder inequality, we observe that the regularity we need for correctly defining the non-linear term* $\mathcal{M}_\beta(\cdot,\cdot)$ *is* $\mathbf{L}^3(\Omega)$*. The space* $\mathbf{Z}$*,endowed with the norm* $\|\mathbf{v}\|_{\mathbf{Z}}^2 = \|\mathbf{v}\|_{L^3}^2 + \|\nabla\cdot\mathbf{v}\|_{L^2}^2$*, is a subspace of* $\mathbf{H}(\mathrm{div}, \Omega)$*.*

3 Discretization

This section introduces the dG–dG–dG and RT–dG–dG discretizations of problem (2). In both approaches, discontinuous elements are employed for the pressure and temperature unknowns. For the velocity, the first approach uses dG schemes, while the second employs RT elements.

3.1 Preliminaries

We start by introducing a subdivision $\mathcal{T}_h$ of the computational domain Ω made of disjoint open polytopal elements. We remark that, in the general case, the dG method supports general polytopal meshes, cf. e.g., [4, 14, 22, 24]). We define an interface as the intersection of the $(d-1)$ -dimensional facets of two neighbouring elements. If $d = 3$, we further assume that each interface consists of a general polygon, which may be decomposed into a set of co-planar triangles. We denote with $\mathcal{F}$, $\mathcal{F}_I$, and $\mathcal{F}_B$ the set of faces, interior faces, and boundary faces, respectively. Following [22, 24], we introduce the following definition.

Definition 3.1 (Polytopal regular mesh [22, 24])**.** A mesh $\mathcal{T}_h$ is said to be polytopal regular if $\forall \kappa \in \mathcal{T}_h$, there exist a set of non-overlapping d-dimensional simplices contained in κ – denoted by $\{S_\kappa^F\}_{F\subset\partial\kappa}$ – such that, for any face $F \subset \partial\kappa$, the following condition holds: $h_\kappa \lesssim d\ |S_\kappa^F|\ |F|^{-1}$.

We next introduce the mesh assumptions.

Assumption 3.1. Given $\{\mathcal{T}_h\}_h, h > 0$, we assume that the following properties are uniformly satisfied:

A.1 $\mathcal{T}_h$ is polytopal-regular in the sense of Defintion 3.1;

A.2 For neighbouring elements $\kappa^+, \kappa^- \in \mathcal{T}_h$, hp-local bounded variation property holds, i.e. $h_{\kappa^+} \lesssim h_{\kappa^-} \lesssim h_{\kappa^+}$, $p_{\kappa^+} \lesssim p_{\kappa^-} \lesssim p_{\kappa^+}$.

Note that the bounded variation hypothesis **A.2** is introduced to avoid technicalities. Under **A.1** the following inequality (*trace-inverse* inequality) holds [23]:

$$\|v\|_{L^q(\partial\kappa)} \lesssim h_\kappa^{-\frac{1}{q}}\, \ell_\kappa^{\frac{2}{q}}\, \|v\|_{L^q(\kappa)} \quad \forall v \in \mathbb{P}^\ell(\kappa), \tag{3}$$

where $\mathbb{P}^\ell(\kappa)$ is the space of polynomials of maximum degree equal to ℓ in κ and the hidden constant is independent of ℓ, h, the number of faces per element, and the relative size of a face compared to the diameter of the element it belongs to.

We also introduce the average and jump operators. We start by defining them on each interface $F \in \mathcal{F}_I$ shared by the elements $\kappa^\pm$ as in [13]:

$$[\![a]\!] = a^+\mathbf{n}^+ + a^-\mathbf{n}^-, \quad [\![\mathbf{a}]\!] = \mathbf{a}^+ \odot \mathbf{n}^+ + \mathbf{a}^- \odot \mathbf{n}^-, \quad [\![\mathbf{a}]\!]_n = \mathbf{a}^+ \cdot \mathbf{n}^+ + \mathbf{a}^- \cdot \mathbf{n}^-,$$
$$\{\!\{a\}\!\} = \frac{a^+ + a^-}{2}, \qquad \{\!\{\mathbf{a}\}\!\} = \frac{\mathbf{a}^+ + \mathbf{a}^-}{2}, \qquad \{\!\{\mathbf{A}\}\!\} = \frac{\mathbf{A}^+ + \mathbf{A}^-}{2},$$

where $\mathbf{a} \odot \mathbf{n} = \mathbf{a}\mathbf{n}^T$, and a, $\mathbf{a}$, $\mathbf{A}$ are scalar-, vector-, and tensor-valued functions, respectively. The notation $(\cdot)^\pm$ is used for the trace on F taken within the interior of $\kappa^\pm$ and $\mathbf{n}^\pm$ is the outer normal vector to $\partial\kappa^\pm$. On boundary faces $F \in \mathcal{F}_B$, we set

$$[\![a]\!] = a\mathbf{n}, \quad \{\!\{a\}\!\} = a, \quad [\![\mathbf{a}]\!] = \mathbf{a} \odot \mathbf{n}, \quad \{\!\{\mathbf{a}\}\!\} = \mathbf{a}, \quad [\![\mathbf{a}]\!]_n = \mathbf{a} \cdot \mathbf{n}, \quad \{\!\{\mathbf{A}\}\!\} = \mathbf{A}.$$

We introduce some further notation for the RT discretization space [17]. Let us now assume that $\mathcal{T}_h$ is made of a conforming, shape-regular simplicial elements. We start by considering $\mathbb{P}^\ell(\kappa) = \left(\mathbb{P}^\ell(\kappa)\right)^d$ the space of piecewise polynomial vectors of degree ℓ defined on κ. The local RT space $\mathbb{RT}^\ell(\kappa)$ [34] is defined as

$$\mathbb{RT}^\ell(\kappa) = \left\{ \mathbf{v} \in \left(\mathbb{P}^\ell(\kappa) + \mathbf{x}\mathbb{P}^\ell(\kappa) \right) : \ \mathbf{v}\cdot\mathbf{n} \in R_\ell(\partial\kappa) \right\},$$

with $\mathbf{x} = (x_1, x_2, \ldots, x_d)$ and $R_\ell(\partial\kappa)$ being the space of $L^2(\partial\kappa)$ functions which are piecewise polynomials of degree ℓ on each of the faces of κ.

Finally, for the sake of simplicity, we assume that the heat conductivity $\mathbf{\Theta}$ and the permeability $\mathbf{K}$ are element-wise constant. Then, we can introduce the following quantity: $\Theta_\kappa = \left(|\sqrt{\mathbf{\Theta}|_\kappa}|_2^2 \right)$, where $|\cdot|_2$ is the ℓ^2-norm in $\mathbb{R}^{d\times d}$. This assumption is reasonable in the context of geophysics, e.g. for groundwater flow models, where the data are obtained via local measurements.

3.2 The dG-dG-dG discrete formulation

In this section, we introduce the dG-dG-dG scheme. Given $\ell, m \geq 1$ such that $\ell + 1 \geq m$, we define:

$$V_h^\ell = \left\{ S \in L^2(\Omega) : S|_\kappa \in \mathbb{P}^\ell(\kappa)\ \forall \kappa \in \mathcal{T}_h \right\}, \quad \mathbf{V}_h^\ell = \left[V_h^\ell \right]^d,$$
$$W_h^m = \left\{ q \in L^2(\Omega) : q|_\kappa \in \mathbb{P}^m(\kappa)\ \forall \kappa \in \mathcal{T}_h \right\}.$$

The dG-dG-dG discretization of problem (2) reads: *find* $(\mathbf{u}_h, p_h, T_h) \in \mathbf{V}_h^\ell \times W_h^m \times V_h^\ell$ *such that* $\forall (\mathbf{v}_h, q_h, S_h) \in \mathbf{V}_h^\ell \times W_h^m \times V_h^\ell$ *it holds:*

$$\begin{aligned} &\mathcal{M}_\nu(T_h, \mathbf{u}_h, \mathbf{v}_h) + \mathcal{M}_\beta(\mathbf{u}_h, \mathbf{u}_h, \mathbf{v}_h) - \mathcal{B}_h(p_h, \mathbf{v}_h) + \mathcal{B}_h(q_h, \mathbf{u}_h) + \mathcal{A}_h(T_h, S_h) \\ &+ \mathcal{C}_h(\mathbf{u}_h, T_h, S_h) + \mathcal{D}_u(\mathbf{u}_h, \mathbf{v}_h) + \mathcal{D}_p(p_h, q_h) = ((\mathbf{f}, g), (\mathbf{v}_h, S_h)), \end{aligned} \tag{4}$$

where the discrete bilinear and trilinear forms are defined by:

$$\begin{aligned} \mathcal{A}_h(T, S) &= (\mathbf{\Theta}\nabla_h T, \nabla_h S) - \sum_{F\in\mathcal{F}} \int_F \left(\{\!\{ \mathbf{\Theta}\nabla_h T \}\!\} \cdot [\![S]\!] + [\![T]\!] \cdot \{\!\{ \mathbf{\Theta}\nabla_h S \}\!\} - \sigma [\![T]\!] \cdot [\![S]\!] \right), \\ \mathcal{B}_h(q, \mathbf{v}) &= -(q, \nabla_h \cdot \mathbf{v}) + \sum_{F\in\mathcal{F}_I} \int_F \{\!\{ q \}\!\} \cdot [\![\mathbf{v}]\!]_n, \\ \mathcal{C}_h(\mathbf{u}, T, S) &= \ (\mathbf{u}\cdot\nabla_h T, S) + \frac{1}{2}(\nabla_h \cdot \mathbf{u}\, T, S) \\ &\quad - \sum_{F\in\mathcal{F}_I} \int_F \left(\{\!\{ \mathbf{u} \}\!\} \cdot [\![T]\!] \right) \{\!\{ S \}\!\} - \frac{1}{2} \sum_{F\in\mathcal{F}_I} \int_F [\![\mathbf{u}]\!]_n \cdot \{\!\{ T\, S \}\!\} \\ &\quad + \frac{1}{2} \sum_{F\in\mathcal{F}} \int_F |\{\!\{ \mathbf{u} \}\!\} \cdot \mathbf{n}|\, [\![T]\!] \cdot [\![S]\!] - \frac{1}{2} \sum_{F\in\mathcal{F}_B} \int_F (\mathbf{u}\cdot\mathbf{n})\, T\, S \\ \mathcal{D}_u(\mathbf{u}, \mathbf{v}) &= \sum_{F\in\mathcal{F}_I} \int_F \xi\, [\![\mathbf{u}]\!]_n \cdot [\![\mathbf{v}]\!]_n, \\ \mathcal{D}_p(p, q) &= \sum_{F\in\mathcal{F}_I} \int_F \varrho\, [\![p]\!]\, [\![v]\!]. \end{aligned} \tag{5}$$

For all $w \in V_h^\ell$ and $\mathbf{w} \in \mathbf{V}_h^\ell$, $\nabla_h w$ and $\nabla_h \cdot \mathbf{w}$ denote the broken differential operators whose restrictions to each element $\kappa \in \mathcal{T}_h$ are defined as $\nabla w_{|\kappa}$ and $\nabla \cdot \mathbf{w}_{|\kappa}$, respectively. The stabilization functions

$\sigma, \xi, \varrho \in L^\infty(\mathcal{F}_h)$ appearing in (5) are defined according to [12, 23, 29, 40] as:

$$\sigma = \begin{cases} \alpha_1 \max\limits_{\kappa \in \{\kappa^+, \kappa^-\}} \left(\dfrac{\overline{\Theta}_\kappa \, \ell^2}{h_\kappa} \right) & F \in \mathcal{F}_I, \\ \alpha_1 \overline{\Theta}_\kappa \dfrac{\ell^2}{h_\kappa} & F \in \mathcal{F}_B, \end{cases} \quad \xi = \begin{cases} \alpha_2 \max\limits_{\kappa \in \{\kappa^+, \kappa^-\}} \left(\dfrac{\ell^2}{h_\kappa} \right) & F \in \mathcal{F}_I, \\ \alpha_2 \dfrac{\ell^2}{h_\kappa} & F \in \mathcal{F}_B, \end{cases}$$
$$\varrho = \begin{cases} \alpha_3 \min\limits_{\kappa \in \{\kappa^+, \kappa^-\}} \left(\dfrac{h_\kappa}{m} \right) & F \in \mathcal{F}_I, \\ \alpha_3 \dfrac{h_\kappa}{m} & F \in \mathcal{F}_B, \end{cases} \tag{6}$$

where $\alpha_1, \alpha_2, \alpha_3 \in \mathbb{R}$ are positive constants to be properly defined and h_κ is the diameter of the element $\kappa \in \mathcal{T}_h$.

To handle the non-linear convective term in the temperature equation, we consider the so-called Temam's modification of the trilinear form that classically models the non-linear advection term. This modification aims to recover the skew-symmetry property of the trilinear form that, in the semi-discrete framework, is generally lost. Indeed, in this framework, the convective velocity is not divergence-free, but only weakly divergence-free. To this aim, we add two consistent terms to the trilinear form. Indeed, we can see the trilinear form $\mathcal{C}$ appearing in (5) as:

$$\mathcal{C}_h(\mathbf{u}, T, S) = \widetilde{\mathcal{C}}_h(\mathbf{u}, T, S) + \frac{1}{2}(\nabla_h \cdot \mathbf{u}\, T, S) - \frac{1}{2} \sum_{F \in \mathcal{F}_I} \int_F [\![\mathbf{u}]\!]_n \cdot \{\!\{T\, S\}\!\},$$

where $\widetilde{\mathcal{C}}_h(\mathbf{u}, T, S)$ is the dG-form that discretizes the convection operator with upwind and inflow stabilizations [19]. At the same time, the last two terms are two consistent terms of Temam's modification. We recall the following result.

Lemma 3.1. *For all $\mathbf{v} \in \mathbf{V}_h^\ell$, for all $S \in V_h^\ell$ it holds:*

$$\mathcal{C}_h(\mathbf{v}, S, S) = \frac{1}{2} \sum_{F \in \mathcal{F}_I} \int_F |\{\!\{\mathbf{v}\}\!\} \cdot \mathbf{n}| \, [\![S]\!]^2 + \frac{1}{2} \sum_{F \in \mathcal{F}_B} \int_F (|\mathbf{v} \cdot \mathbf{n}| - \mathbf{v} \cdot \mathbf{n}) \, S^2 \geq 0.$$

We remark that in Lemma 3.1 we do not recover the skew-symmetry of the trilinear form due to the presence of the stabilization terms. However, thanks to the Temam trick, we can control the sign of $\mathcal{C}_h$.

Remark 3.1. *In the discrete formulation above, we consider the same polynomial degree for $\mathbf{V}_h^\ell$ and V_h^ℓ, because we are interested in approximation schemes yielding the same accuracy for the velocity and temperature. To ensure inf-sup stability of the discrete system, we need the pressure field p_h to belong to W_h^m, with $\ell + 1 \geq m$.*

Remark 3.2. *In the bilinear forms $\mathcal{B}_h$ and $\mathcal{D}_u$, the interface terms are summed only on the set of internal faces $\mathcal{F}_I$ of the mesh. This is due to the choice of the boundary conditions (i.e., Dirichlet boundary conditions for the pressure field).*

Remark 3.3. *In the trilinear form $\mathcal{C}_h$, we have added two stabilization terms in the spirit of [19] for making the scheme robust to the advection-dominated regime. We highlight that this configuration is relevant in this context, as – with the DF law – we intend to describe phenomena in which the velocity of the flow is high.*

3.3 The RT-dG-dG discrete problem

In this section, we introduce the RT-dG-dG discretization, highlighting the differences with respect to the RT-dG-dG one. Given the polynomial degrees of approximation ℓ, m, and the discrete spaces W_h^m, V_h^ℓ defined as before, we introduce the following discrete space for the velocity field:

$$\mathbf{Z}_h^m = \{\mathbf{v} \in \mathbf{Z} : \mathbf{v}|_\kappa \in \mathbb{RT}^m(\kappa) \ \forall \kappa \in \mathcal{T}_h\}.$$

Then, the RT-dG-dG discretization of problem (2) reads: *find* $(\mathbf{u}_h, p_h, T_h) \in \mathbf{Z}_h^m \times W_h^m \times V_h^\ell$ *such that* $\forall (\mathbf{v}_h, q_h, S_h) \in \mathbf{Z}_h^m \times W_h^m \times V_h^\ell$ *it holds:*

$$\begin{aligned} &\mathcal{M}_\nu(T_h, \mathbf{u}_h, \mathbf{v}_h) + \mathcal{M}_\beta(\mathbf{u}_h, \mathbf{u}_h, \mathbf{v}_h) - \widehat{\mathcal{B}}_h(p_h, \mathbf{v}_h) + \widehat{\mathcal{B}}_h(q_h, \mathbf{u}_h) \\ &+ \mathcal{A}_h(T_h, S_h) + \widehat{\mathcal{C}}_h(\mathbf{u}_h, T_h, S_h) = ((\mathbf{f}, g), (\mathbf{v}_h, S_h)), \end{aligned} \tag{7}$$

with

$$\begin{aligned} &\widehat{\mathcal{B}}_h(\varphi, \mathbf{v}) = -(\varphi, \nabla_h \cdot \mathbf{v}) = \mathcal{B}_h(\varphi, \mathbf{v}), \\ &\widehat{\mathcal{C}}_h(\mathbf{v}, T, S) = (\mathbf{v} \cdot \nabla_h T, S) + \frac{1}{2}(\nabla_h \cdot \mathbf{v}\, T, S) - \sum_{F \in \mathcal{F}_I} \int_F (\mathbf{v} \cdot [\![T]\!])\, \{\!\{S\}\!\} \\ &\qquad + \frac{1}{2} \sum_{F \in \mathcal{F}} \int_F |\mathbf{v} \cdot \mathbf{n}|\, [\![T]\!] \cdot [\![S]\!] - \frac{1}{2} \sum_{F \in \mathcal{F}_B} \int_F (\mathbf{v} \cdot \mathbf{n})\, T\, S = \mathcal{C}_h(\mathbf{v}, T, S) \end{aligned}$$

for all $\mathbf{v} \in \mathbf{Z}_h^m$, $\varphi \in W_h^m$, and $T, S \in V_h^\ell$, and where the remaining bilinear and trilinear forms are defined as before. Notice that $[\![\mathbf{z}]\!]_n = 0$ for $\mathbf{z} \in \mathbf{Z}_h^m$, which implies that some interface terms vanish. For ensuring the inf-sup stability, we take W_h^m as discrete space for the pressure, where m is the degree of the RT space of the velocity.

Remark 3.4. *We observe that the discrete space* $\mathbf{Z}_h^m$ *is a subspace of* $\mathbf{V}_h^\ell$ *for* $\ell \geq m+1$. *Following this observation, in Section 4, the stability analysis is carried out for the dG-dG-dG formulation, and all the results, naturally hold for the RT-dG-dG scheme as well. Moreover, the Brezzi-Douglas-Marini (BDM) discrete spaces [17, 21] can be seen as subspaces of dG-discrete spaces as well. Then, all the results presented in this article can be extended to a BDM-dG-dG scheme.*

3.4 Linearization

For tackling the non-linear terms appearing in (4) (and in (7)), we introduce a fixed-point iterative algorithm. Let $k \geq 1$ be the iteration step and let $\mathbf{u}_h^{k-1}, T_h^{k-1}$ be the approximated velocity and temperature fields computed at the $(k-1)^{\text{th}}$ iteration, respectively. Then, at the k^{th} step we solve: *find* $(\mathbf{u}_h^k, p_h^k, T_h^k) \in \mathbf{V}_h^\ell \times W_h^m \times V_h^\ell$ *such that* $\forall (\mathbf{v}_h, q_h, S_h) \in \mathbf{V}_h^\ell \times W_h^m \times V_h^\ell$ *it holds:*

$$\begin{aligned} &\mathcal{M}_\nu(T_h^{k-1}, \mathbf{u}_h^k, \mathbf{v}_h) + \mathcal{M}_\beta(\mathbf{u}_h^{k-1}, \mathbf{u}_h^k, \mathbf{v}_h) - \mathcal{B}_h(p_h^k, \mathbf{v}_h) + \mathcal{B}_h(q_h, \mathbf{u}_h^k) + \mathcal{A}_h(T_h^k, S_h) \\ &+ \mathcal{C}_h(\mathbf{u}_h^{k-1}, T_h^k, S_h) + \mathcal{D}_u(\mathbf{u}_h^k, \mathbf{v}_h) + \mathcal{D}_p(p_h^k, q_h) = ((\mathbf{f}, g), (\mathbf{v}_h, S_h)). \end{aligned} \tag{8}$$

Remark 3.5. *We observe that the fluid and heat problems are decoupled. Indeed, a splitting of the two physics is naturally induced by the linearization scheme (8).*

The linearization algorithm is initialized by solving the linear flow problem and using the resulting velocity field in the temperature equation. Finally, the updated velocity and temperature fields are fed to the next iteration of the scheme. The convergence of algorithm (8) is established in Section 4 under suitable assumptions.

4 Theoretical analysis

The aim of this section is to establish a stability estimate for the non-linear problems (4) and (7), and to prove the convergence of the iterative algorithm (8).

4.1 Stability estimates

We focus on problem (4) and stress again that these results hold automatically for problem (7).

We start by introducing notation and results that will be used in the analysis. First, the energy norms are defined $\forall (\mathbf{v}, q, S) \in \mathbf{V}_h^\ell \times W_h^m \times V_h^\ell$ as:

$$
\begin{aligned}
|||\mathbf{v}|||_{dG,\mathrm{div}} &= \|\mathbf{v}\| + \|\mathbf{v}\|_{L^3} + \|\nabla_h\cdot\mathbf{v}\| + \left(\sum_{F\in\mathcal{F}_I}\|\xi^{1/2}[\![\mathbf{v}]\!]_n\|_F^2\right)^{1/2},\\
\|S\|_{dG,T}^2 &= \|\sqrt{\boldsymbol{\Theta}}\,\nabla_h S\|^2 + \sum_{F\in\mathcal{F}}\|\sigma^{1/2}[\![S]\!]\|_F^2,\\
\|(\mathbf{v},q,S)\|_{\mathcal{E}}^2 &= \|\mathbf{v}\|^2 + \|\mathbf{v}\|_{L^3}^3 + \|\nabla_h\cdot\mathbf{v}\|^2 + \sum_{F\in\mathcal{F}_I}\|\xi^{1/2}\,[\![\mathbf{v}]\!]_n\|_F^2 + \mathbb{B}^2\,\|q\|^2 + \|S\|_{dG,T}^2.
\end{aligned}
\tag{9}
$$

Next, we state the following technical lemmata.

Lemma 4.1. *Let Assumptions 2.1 and 3.1 be satisfied and assume that the parameter α_1 appearing in (6) is chosen large enough. Then, the following bounds hold:*

$$
\mathcal{A}_h(T,S) \lesssim \|T\|_{dG,T}\|S\|_{dG,T}, \qquad \mathcal{A}_h(T,T) \gtrsim \|T\|_{dG,T}^2 \qquad \forall\, T,S\in V_h^\ell,
$$

where the hidden constants do not depend on the material properties and the discretization parameters.

For all $\mathbf{v}\in\mathbf{V}_h^\ell$, let $\|\mathbf{v}\|_{dG} = \|\nabla_h\mathbf{v}\|^2 + \sum_{F\in\mathcal{F}}\|\xi^{1/2}[\![\mathbf{v}]\!]\|_F^2$, we recall the following result and refer to [8] for the proof.

Lemma 4.2. *[8] Let Assumption 3.1 hold and let the polynomial degrees ℓ and m satisfy $\ell+1\geq m$. Then, there exists a positive constant $\mathbb{B}$ independent of the mesh size h (but possibly dependent on ℓ and m) such that:*

$$
\sup_{\mathbf{0}\neq\mathbf{v}_h\in\mathbf{V}_h^\ell}\frac{\mathcal{B}_h(\mathbf{v}_h,q_h)}{\|\mathbf{v}_h\|_{dG}} + \mathcal{D}_p(q_h,q_h)^{\frac{1}{2}} \geq \mathbb{B}\|q_h\| \qquad \forall q_h\in W_h^m. \tag{10}
$$

The following result is an extension of Lemma 4.2 and it is needed for controlling the L^2-norm of the pressure field.

Proposition 4.1. *Under the assumptions of Lemma 4.2, there exists a positive constant $\mathbb{B}$ independent of the mesh size h (but possibly dependent on ℓ and m) such that:*

$$
\sup_{\mathbf{0}\neq\mathbf{v}_h\in\mathbf{V}_h^\ell}\frac{\mathcal{B}_h(\mathbf{v}_h,q_h)}{|||\mathbf{v}_h|||_{dG,\mathrm{div}}} + \mathcal{D}_p(q_h,q_h)^{\frac{1}{2}} \gtrsim \mathbb{B}\|q_h\| \qquad \forall q_h\in W_h^m. \tag{11}
$$

Proof. We start the proof by observing that:

$$
|||\mathbf{v}|||_{dG,\mathrm{div}} \lesssim \|\mathbf{v}\|_{dG} \qquad \forall\,\mathbf{v}\in\mathbf{V}_h^\ell. \tag{12}
$$

Indeed, the first two terms of $|||\mathbf{v}|||_{dG,\mathrm{div}}$ are controlled via Poincaré-Sobolev inequalities [20, Theorem 1.6], while the third and the fourth term are trivially controlled by terms of $\|\mathbf{v}\|_{dG}$. Then, the thesis directly follows from (10) and (12). □

The next result is instrumental for the derivation of an *a-priori* stability estimate for the non-linear discrete problem. The target of the Lemma is to obtain and prove two basic estimates.

Lemma 4.3. *Let Assumptions 2.1 and 3.1 be satisfied and assume that the parameter α_1 appearing in (6) is chosen large enough. Then, the solution $(\mathbf{u}_h,p_h,T_h)\in\mathbf{V}_h^\ell\times W_h^m\times V_h^\ell$ to problem (4) satisfies the following estimates:*

$$
(i)\ \left\|\sqrt{\frac{\nu_m}{2k_M}}\,\mathbf{u}_h\right\|^2 + \|\sqrt[3]{\beta}\,\mathbf{u}_h\|_{L^3}^3 + \frac{\alpha_T}{2}\|T_h\|_{dG,T}^2 \leq \frac{k_M}{2\nu_m}\|\mathbf{f}\|^2 + \frac{C_p^2}{2\alpha_T\theta_m}\|g\|^2, \tag{13a}
$$

$$
\begin{aligned}
(ii)\ &\left\|\sqrt{\frac{\nu_m}{2k_M}}\,\mathbf{u}_h\right\|^2 + \|\sqrt[3]{\beta}\,\mathbf{u}_h\|_{L^3}^3 + \frac{1}{3}\|\nabla_h\cdot\mathbf{u}_h\|^2 + \frac{1}{4}\sum_{F\in\mathcal{F}_I}\|\xi^{1/2}\,[\![\mathbf{u}_h]\!]_n\|_F^2\\
&+ \frac{\alpha_T}{2}\|T_h\|_{dG,T}^2 \leq \mathcal{M}_\nu(T_h,\mathbf{u}_h,\mathbf{u}_h) + \mathcal{M}_\beta(\mathbf{u}_h,\mathbf{u}_h,\mathbf{u}_h) + \mathcal{A}_h(T_h,T_h)\\
&+ \mathcal{C}_h(\mathbf{u}_h,T_h,T_h) + \mathcal{D}_u(\mathbf{u}_h,\mathbf{u}_h).
\end{aligned}
\tag{13b}
$$

where C_p is the constant of the Poincaré inequality.

Proof. We start the proof by taking $(\mathbf{v}_h, q_h, S_h) = (\mathbf{u}_h, p_h, T_h)$ as test functions in (4). We obtain:

$$\begin{aligned}&\mathcal{M}_\nu(T_h, \mathbf{u}_h, \mathbf{u}_h) + \mathcal{M}_\beta(\mathbf{u}_h, \mathbf{u}_h, \mathbf{u}_h) + \mathcal{A}_h(T_h, T_h) + \mathcal{C}_h(\mathbf{u}_h, T_h, T_h)\\ &+ \mathcal{D}_u(\mathbf{u}_h, \mathbf{u}_h) + \mathcal{D}_p(p_h, p_h) = ((\mathbf{f}, g), (\mathbf{u}_h, T_h)).\end{aligned} \tag{14}$$

Now, we observe that, by using Assumption 2.1, Lemma 4.1, and Lemma 3.1 the following results hold:

$$\begin{aligned}&\mathcal{M}_\nu(T_h, \mathbf{u}_h, \mathbf{u}_h) \geq \left\| \sqrt{\nu_m/k_M}\, \mathbf{u}_h \right\|^2, && \mathcal{M}_\beta(\mathbf{u}_h, \mathbf{u}_h, \mathbf{u}_h) = \| \sqrt[3]{\beta}\, \mathbf{u}_h\|_{L^3}^3,\\ &\mathcal{A}_h(T_h, T_h) \geq \alpha_T \|T_h\|_{dG,T}^2, && \mathcal{C}_h(\mathbf{u}_h, T_h, T_h) \geq 0,\\ &\mathcal{D}_u(\mathbf{u}_h, \mathbf{u}_h) = \sum_{F\in\mathcal{F}_I} \|\xi^{1/2}\, [\![\mathbf{u}_h]\!]_n\|_F^2 \geq 0, && \mathcal{D}_p(p_h, p_h) = \sum_{F\in\mathcal{F}_I} \int_F \varrho [\![p_h]\!]^2 \geq 0.\end{aligned} \tag{15}$$

By exploiting (15) and using Cauchy-Schwarz and Young inequalities for the right hand side of (14), we obtain (13a). For proving (13b), we need to control also the divergence of the discrete velocity field. To this aim, we test problem (4) with $(\mathbf{v}_h, q_h, S_h) = (\mathbf{0}, -\nabla_h \cdot \mathbf{u}_h, 0)$ and we find:

$$\mathcal{B}_h(-\nabla_h \cdot \mathbf{u}_h, \mathbf{u}_h) + \mathcal{D}_p(p_h, \mathbf{u}_h) = 0.$$

Now, by using Cauchy-Schwarz, Young, and trace-inverse inequality (cf. (3)), we get:

$$\left(1 - \frac{1}{2\epsilon_1} - \frac{1}{2\epsilon_2}\right) \|\nabla_h \cdot \mathbf{u}_h\|^2 - \frac{\epsilon_1}{2} \sum_{F\in\mathcal{F}_I} \|\xi^{1/2}\, [\![\mathbf{u}_h]\!]_n\|_F^2 - \frac{\epsilon_2}{2} \sum_{F\in\mathcal{F}_I} \int_F \varrho [\![p_h]\!]^2 \leq 0. \tag{16}$$

Last, we fix $\epsilon_1 = \epsilon_2 = 3/2$ and we combine (15) and (16) to obtain (13b). □

We are now ready to state the main result of this section, establishing the stability estimate for the non-linear discrete Darcy-Forchheimer flow problem coupled with an advection-diffusion equation for the temperature.

Theorem 4.1. Let the assumptions of Lemmata 4.1, 4.1, and 4.3 be satisfied. Then, the solution $(\mathbf{u}_h, p_h, T_h) \in \mathbf{V}_h^\ell \times W_h^m \times V_h^\ell$ to (4) satisfies the a-priori bound

$$\| (\mathbf{u}_h, p_h, T_h) \|_{\mathcal{E}}^2 \lesssim \|\mathbf{f}\|^2 + \|g\|^2 + \left(\|\mathbf{f}\|^2 + \|g\|^2\right)^{\frac{2}{3}} + \left(\|\mathbf{f}\|^2 + \|g\|^2\right)^{\frac{4}{3}},$$

where the hidden constant is independent of the mesh size h.

Proof. The first step of the proof consists in using the inf-sup condition (cf. Lemma 4.1) to find a bound for the pressure field. Taking $(\mathbf{v}_h, q_h, S_h) = (\mathbf{v}_h, 0, 0)$ in (4) we have:

$$\mathcal{B}_h(p_h, \mathbf{v}_h) = \mathcal{M}_\nu(T_h, \mathbf{u}_h, \mathbf{v}_h) + \mathcal{M}_\beta(\mathbf{u}_h, \mathbf{u}_h, \mathbf{v}_h) + \mathcal{D}_u(\mathbf{u}_h, \mathbf{v}_h) - (\mathbf{f}, \mathbf{v}_h).$$

By plugging the previous identity into (11) and by using Cauchy-Schwarz and Hölder inequalities we obtain:

$$\begin{aligned}\frac{\mathbb{B}^2}{2} \|p_h\|^2 &\leq \left(\sup_{\mathbf{0}\neq\mathbf{v}_h\in\mathbf{V}_h^\ell} \frac{\mathcal{M}_\nu(T_h, \mathbf{u}_h, \mathbf{v}_h) + \mathcal{M}_\beta(\mathbf{u}_h, \mathbf{u}_h, \mathbf{v}_h) + \mathcal{D}_u(\mathbf{u}_h, \mathbf{v}_h) - (\mathbf{f}, \mathbf{v}_h)}{|||\mathbf{v}_h|||_{dG,\mathrm{div}}} \right)^2\\ &\quad + \mathcal{D}_p(p_h, p_h)\\ &\leq \|(\nu_M/k_m)\, \mathbf{u}_h\|^2 + \|\sqrt{\beta}\mathbf{u}_h\|_{L^3}^4 + |||\mathbf{u}_h|||_{dG,\mathrm{div}}^2 + \|\mathbf{f}\|^2 + \mathcal{D}_p(p_h, p_h),\end{aligned} \tag{17}$$

where the second bound follows observing that

$$\mathcal{M}_\beta(\mathbf{u}_h, \mathbf{u}_h, \mathbf{v}_h) = (\beta|\mathbf{u}_h|\mathbf{u}_h, \mathbf{v}_h) \leq \|\beta\, |\mathbf{u}_h|\mathbf{u}_h\|_{L^{3/2}} \|\mathbf{v}_h\|_{L^3} \leq \|\sqrt{\beta}\mathbf{u}_h\|_{L^3}^2\, |||\mathbf{v}_h|||_{dG,\mathrm{div}}.$$

In the second step of the proof, we find a bound for $\|\sqrt{\beta}\, \mathbf{u}_h\|_{L^3}^4$. From (13a), we can easily see that:

$$\|\sqrt{\beta}\, \mathbf{u}_h\|_{L^3}^3 = \sqrt{\beta} \|\sqrt[3]{\beta}\, \mathbf{u}_h\|_{L^3}^3 \leq \frac{k_M\sqrt{\beta}}{2\nu_m} \|\mathbf{f}\|^2 + \frac{C_p^2\sqrt{\beta}}{2\alpha_T\theta_m} \|g\|^2,$$

and therefore

$$\|\sqrt{\beta}\,\mathbf{u}_h\|_{L^3}^4 \leq \left(\frac{k_M\sqrt{\beta}}{2\nu_m}\|\mathbf{f}\|^2 + \frac{C_p^2\sqrt{\beta}}{2\alpha_T\theta_m}\|g\|^2\right)^{\frac{4}{3}}. \tag{18}$$

We now consider (13b), we add $(\epsilon\mathbb{B}^2/2)\,\|p_h\|^2$ to the left and right hand side, and we use (17):

$$\begin{aligned}
&\left\|\sqrt{\frac{\nu_m}{2k_M}}\,\mathbf{u}_h\right\|^2 + \|\sqrt[3]{\beta}\,\mathbf{u}_h\|_{L^3}^3 + \frac{1}{3}\|\nabla_h\cdot\mathbf{u}_h\|^2 + \frac{1}{4}\sum_{F\in\mathcal{F}_I}\|\xi^{1/2}\,[\![\mathbf{u}_h]\!]_n\|_F^2 + \frac{\alpha_T}{2}\|T_h\|_{dG,T}^2 \\
&+ \frac{\epsilon\mathbb{B}^2}{2}\,\|p_h\|^2 \leq \mathcal{M}_\nu(T_h,\mathbf{u}_h,\mathbf{u}_h) + \mathcal{M}_\beta(\mathbf{u}_h,\mathbf{u}_h,\mathbf{u}_h) + \mathcal{A}_h(T_h,T_h) + \mathcal{C}_h(\mathbf{u}_h,T_h,T_h) \\
&+ \mathcal{D}_u(\mathbf{u}_h,\mathbf{u}_h) + \mathcal{D}_p(p_h,p_h) + \epsilon\left(\left\|\frac{\nu_M}{k_m}\,\mathbf{u}_h\right\|^2 + \|\sqrt{\beta}\mathbf{u}_h\|_{L^3}^4 + |||\mathbf{u}_h|||_{dG,\mathrm{div}}^2 + \|\mathbf{f}\|^2\right).
\end{aligned}$$

We observe that the first six terms at right hand side are equal to $((\mathbf{f},g),(\mathbf{u}_h,T_h))$ (cf. (14)), we apply Cauchy-Schwarz and Young inqualities on it and we exploit (18) for bounding the eighth term at right hand side:

$$\begin{aligned}
&\left\|\sqrt{\frac{\nu_m}{4k_M}}\,\mathbf{u}_h\right\|^2 + \|\sqrt[3]{\beta}\,\mathbf{u}_h\|_{L^3}^3 + \frac{1}{3}\|\nabla_h\cdot\mathbf{u}_h\|^2 + \frac{1}{4}\sum_{F\in\mathcal{F}_I}\|\xi^{1/2}\,[\![\mathbf{u}_h]\!]_n\|_F^2 + \frac{\alpha_T}{4}\|T_h\|_{dG,T}^2 \\
&+ \frac{\epsilon\mathbb{B}^2}{2}\,\|p_h\|^2 \leq \frac{k_M}{\nu_m}\|\mathbf{f}\|^2 + \frac{C_p^2}{\alpha_T\theta_m}\|g\|^2 + \epsilon\left(\frac{k_M\sqrt{\beta}}{2\nu_m}\|\mathbf{f}\|^2 + \frac{C_p^2\sqrt{\beta}}{2\alpha_T\theta_m}\|g\|^2\right)^{\frac{4}{3}} + \epsilon\|\mathbf{f}\|^2 \\
&+ \epsilon\left(\left\|\frac{\nu_M}{k_m}\,\mathbf{u}_h\right\|^2 + |||\mathbf{u}_h|||_{dG,\mathrm{div}}^2\right).
\end{aligned}$$

Finally, we choose the auxiliary parameter ϵ to be:

$$\epsilon = \frac{1}{4}\,\min\left(\frac{\nu_m\,k_m^2}{4\,k_M\,\nu_M^2}, \frac{1}{3}, \frac{1}{4}\right),$$

we bound the $\|\mathbf{u}_h\|_{L^3}^2$ contribution appearing from the last term of right hand side as done in (18) and this concludes the proof. □

4.2 Convergence of the fixed-point algorithm

The aim of this section is to prove the convergence of the linearization algorithm, cf. Section 3.4. To this aim, we show that the difference of approximate solutions at two successive iterations defines is a contracting sequence. Let $(\mathbf{u}_h^{k+1},p_h^{k+1},T_h^{k+1})$ and $(\mathbf{u}_h^k,p_h^k,T_h^k)$ be the solutions to (8) at the $(k+1)^{\text{th}}$ and k^{th} iterations, respectively. For all $k\geq 1$, we define:

$$\boldsymbol{\delta}_{\mathbf{u}}^k = \mathbf{u}^{k+1} - \mathbf{u}^k, \qquad \delta_p^k = p^{k+1} - p^k, \qquad \delta_T^k = T^{k+1} - T^k.$$

Then, it can be observed that $(\boldsymbol{\delta}_{\mathbf{u}}^k,\delta_p^k,\delta_T^k)$ solves the problem:

$$\begin{aligned}
&\mathcal{M}_\nu(T_h^k,\mathbf{u}_h^{k+1},\mathbf{v}_h) - \mathcal{M}_\nu(T_h^{k-1},\mathbf{u}_h^k,\mathbf{v}_h) + \mathcal{M}_\beta(\mathbf{u}_h^k,\mathbf{u}_h^{k+1},\mathbf{v}_h) \\
&- \mathcal{M}_\beta(\mathbf{u}_h^{k-1},\mathbf{u}_h^k,\mathbf{v}_h) - \mathcal{B}_h(\delta_p^k,\mathbf{v}_h) + \mathcal{B}_h(q_h,\boldsymbol{\delta}_{\mathbf{u}}^k) + \mathcal{A}_h(\delta_T^k,S_h) \\
&+ \mathcal{C}_h^t(\mathbf{u}_h^k,T_h^{k+1},S_h) - \mathcal{C}_h^t(\mathbf{u}_h^{k-1},T_h^k,S_h) + \mathcal{D}_u(\boldsymbol{\delta}_{\mathbf{u}}^k,\mathbf{v}) + \mathcal{D}_p(\delta_p^k,q) = 0.
\end{aligned}$$

In the following theorem, we state the conditions under which the fixed-point iterative method converges. We start by observing that, as in this case we are considering the linearized problem instead of the non-linear one, we want to control the error for the velocity field in the following norm:

$$\|\mathbf{v}\|_{dG,\mathrm{div}}^2 = \|\mathbf{v}\|^2 + \|\nabla_h\cdot\mathbf{v}\|^2 + \sum_{F\in\mathcal{F}_I}\|\xi^{1/2}[\![\mathbf{v}]\!]_n\|_F^2 \qquad \forall\ \mathbf{v}\in\mathbf{V}_h^\ell,$$

while the norms for the temperature and pressure fields are the same defined in (9). Moreover, we introduce the auxiliary $\|S\|^2_{dG,3}$-norm of the functions belonging to V_h^ℓ as follows:

$$\|S\|^2_{dG,3} = \|S\|^2_{L^3(\Omega)} + \|\nabla_h S\|^2_{\mathbf{L}^3(\Omega)} + \max_{F\in\mathcal{F}} \max_{\kappa\in\{\kappa^+,\kappa^-\}} \frac{\ell^2}{h_\kappa} \| [\![S]\!] \|^2_{\mathbf{L}^3(F)} \quad \forall\, S \in V_h^\ell.$$

Theorem 4.2. Let the assumptions of Theorem 4.1 be satisfied. Additionally, assume that:

$$\|\mathbf{u}_h^k\|_{\mathbf{L}^\infty} \lesssim \min\left(\frac{\nu_m}{k_M \beta}, \sqrt{\frac{\alpha_T\, \nu_m\, k_m^2}{k_M\, L_\nu^2}}\right) \quad \text{and} \quad \|T_h^k\|_{dG,3} \lesssim \sqrt{\frac{\nu_m\, \theta_M\, \alpha_T}{k_M}} \tag{19}$$

where α_T has been defined in Lemma 4.1. Then, the linearization strategy defined in Section 3.4 converges, namely $\mathbf{V}_h^\ell \times W_h^m \times V_h^\ell \ni (\boldsymbol{\delta}_{\mathbf{u}}^k, \delta_p^k, \delta_T^k) \to \mathbf{0}$ as $k \to \infty$.

Proof. We start the proof by adding and subtracting $\mathcal{M}_\nu(T_h^k, \mathbf{u}_h^k, \mathbf{v}_h)$, $\mathcal{M}_\beta(\mathbf{u}_h^k, \mathbf{u}_h^k, \mathbf{v}_h)$, and $\mathcal{C}_h(\mathbf{u}_h^k, T_h^k, S_h)$ to (20). Then, expanding the trilinear forms we obtain:

$$\begin{aligned}
&\Big((\nu(T_h^k)\mathbf{K}^{-1} + \beta|\mathbf{u}_h^k|)\, \boldsymbol{\delta}_{\mathbf{u}}^k, \mathbf{v}_h\Big) - \mathcal{B}_h(\delta_p^k, \mathbf{v}_h) + \mathcal{B}_h(q_h, \boldsymbol{\delta}_{\mathbf{u}}^k) + \mathcal{A}_h(\delta_T^k, S_h) \\
&+ \mathcal{C}_h(\mathbf{u}_h^k, \delta_T^k, S_h) + \mathcal{D}_u(\boldsymbol{\delta}_{\mathbf{u}}^k, \mathbf{v}) + \mathcal{D}_p(\delta_p^k, q) = -\mathcal{C}_h(\boldsymbol{\delta}_{\mathbf{u}}^{k-1}, T_h^k, S_h) \\
&+ \Big((\nu(T_h^{k-1})\mathbf{K}^{-1} - \nu(T_h^k)\mathbf{K}^{-1} + \beta|\mathbf{u}_h^{k-1}| - \beta|\mathbf{u}_h^k|)\, \mathbf{u}_h^k, \mathbf{v}_h\Big).
\end{aligned} \tag{20}$$

In the second step of the proof, we focus on the fluid flow and incompressibility equations. We consider $(\mathbf{v}_h, q_h, S_h) = (\boldsymbol{\delta}_{\mathbf{u}}^k, \delta_p^k, 0)$ as test functions in (20):

$$\begin{aligned}
&\Big((\nu(T_h^k)\mathbf{K}^{-1} + \beta|\mathbf{u}_h^k|)\, \boldsymbol{\delta}_{\mathbf{u}}^k, \boldsymbol{\delta}_{\mathbf{u}}^k\Big) + \mathcal{D}_u(\boldsymbol{\delta}_{\mathbf{u}}^k, \boldsymbol{\delta}_{\mathbf{u}}^k) + \mathcal{D}_p(\delta_p^k, \delta_p^k) \\
&= \Big((\nu(T_h^{k-1})\mathbf{K}^{-1} - \nu(T_h^k)\mathbf{K}^{-1} + \beta|\mathbf{u}_h^{k-1}| - \beta|\mathbf{u}_h^k|)\, \mathbf{u}_h^k, \boldsymbol{\delta}_{\mathbf{u}}^k\Big).
\end{aligned}$$

We start by noting that $\big((\nu(T_h^k)\mathbf{K}^{-1} + \beta|\mathbf{u}_h^k|)\, \boldsymbol{\delta}_{\mathbf{u}}^k, \boldsymbol{\delta}_{\mathbf{u}}^k\big) \geq \frac{\nu_m}{k_M}\|\mathbf{e}_u^k\|^2$ by Assumption 2.1. Next, we test problem (20) with $(\mathbf{v}_h, q_h, S_h) = (\mathbf{0}, -\nabla_h\cdot\boldsymbol{\delta}_{\mathbf{u}}^k, 0)$ and we obtain

$$\mathcal{B}_h(-\nabla_h\cdot\boldsymbol{\delta}_{\mathbf{u}}^k, \boldsymbol{\delta}_{\mathbf{u}}^k) + \mathcal{D}_p(\delta_p^k, -\nabla_h\cdot\boldsymbol{\delta}_{\mathbf{u}}^k) = 0.$$

By proceeding as in Section 4 (cf. Equation (16)) and using Cauchy-Schwarz and Young inequalities we get

$$\begin{aligned}
&\frac{\nu_m}{2k_M}\|\boldsymbol{\delta}_{\mathbf{u}}^k\|^2 + \|\nabla_h\cdot\boldsymbol{\delta}_{\mathbf{u}}^k\|^2 + \sum_{F\in\mathcal{F}_I} \|\sqrt{\xi}[\![\boldsymbol{\delta}_{\mathbf{u}}^k]\!]_n\|_F^2 + \mathcal{D}_p(\delta_p^k, \delta_p^k) \\
&\qquad \lesssim \frac{2k_M}{\nu_m}\Big\|(\nu(T_h^{k-1})\mathbf{K}^{-1} - \nu(T_h^k)\mathbf{K}^{-1} + \beta|\mathbf{u}_h^{k-1}| - \beta|\mathbf{u}_h^k|)\, \mathbf{u}_h^k\Big\|^2.
\end{aligned} \tag{21}$$

We are left to control the right hand side of (21). To this aim, we use the Lipschitz-continuity of the viscosity coefficient ν (we denote by L_ν the Lipschitz constant) and the triangle inequality to get:

$$\begin{aligned}
&\frac{\nu_m}{2k_M}\|\boldsymbol{\delta}_{\mathbf{u}}^k\|^2 + \|\nabla_h\cdot\boldsymbol{\delta}_{\mathbf{u}}^k\|^2 + \sum_{F\in\mathcal{F}_I} \|\sqrt{\xi}[\![\boldsymbol{\delta}_{\mathbf{u}}^k]\!]_n\|_F^2 + \mathcal{D}_p(\delta_p^k, \delta_p^k) \\
&\qquad \lesssim \frac{4k_M}{\nu_m}\|\mathbf{u}_h^k\|^2_{\mathbf{L}^\infty}\left(\frac{L_\nu^2}{k_m^2}\|\delta_T^{k-1}\|^2_{dG,T} + \beta^2\|\boldsymbol{\delta}_{\mathbf{u}}^{k-1}\|^2\right)
\end{aligned}$$

Now, in the third step of the proof, we focus on the temperature equation. We consider $(\mathbf{v}_h, q_h, S_h) = (\mathbf{0}, 0, \delta_T^k)$ in (20) and we obtain:

$$\mathcal{A}_h(\delta_T^k, \delta_T^k) + \mathcal{C}_h(\mathbf{u}_h^k, \delta_T^k, \delta_T^k) = -\mathcal{C}_h(\boldsymbol{\delta}_{\mathbf{u}}^{k-1}, T_h^k, \delta_T^k),$$

where, due to Lemma 3.1, we have that $\mathcal{C}_h(\mathbf{u}_h^k, \delta_T^k, \delta_T^k) \geq 0$. Then, we are left with:

$$\alpha_T\|\delta_T^k\|^2_{dG,T} \leq -\mathcal{C}_h(\boldsymbol{\delta}_{\mathbf{u}}^{k-1}, T_h^k, \delta_T^k) = \mathcal{I}_1 + \mathcal{I}_2 + \mathcal{I}_3,$$

where, by using Hölder, Poincarè, Young, triangle, and trace-inverse inequalities [20], we get:

$$
\begin{aligned}
\mathcal{I}_1 =& -(\boldsymbol{\delta}_{\mathbf{u}}^{k-1}\cdot\nabla T_h^k,\delta_T^k)-\frac{1}{2}(\nabla_h\cdot\boldsymbol{\delta}_{\mathbf{u}}^{k-1}\,T_h^k,\delta_T^k),\\
&\leq \|\nabla_h T_h^k\|_{\mathbf{L}^3}\|\boldsymbol{\delta}_{\mathbf{u}}^{k-1}\|\|\delta_T^k\|_{L^6}+\frac{1}{2}\|T_h^k\|_{L^3}\|\nabla_h\cdot\boldsymbol{\delta}_{\mathbf{u}}^{k-1}\|\|\delta_T^k\|_{L^6}\\
&\leq \frac{\epsilon}{2}\|\nabla_h T_h^k\|_{\mathbf{L}^3}^2\|\boldsymbol{\delta}_{\mathbf{u}}^{k-1}\|^2+\frac{1}{2\epsilon}\|\delta_T^k\|_{L^6}^2+\frac{\epsilon}{2}\|T_h^k\|_{L^3}^2\|\nabla_h\cdot\boldsymbol{\delta}_{\mathbf{u}}^{k-1}\|^2+\frac{1}{4\epsilon}\|\delta_T^k\|_{L^6}^2\\
&\leq \epsilon\|T_h^k\|_{dG,3}^2\|\boldsymbol{\delta}_{\mathbf{u}}^{k-1}\|_{dG,\mathrm{div}}^2+\frac{3\,C_p}{4\epsilon\,\theta_M}\|\delta_T^k\|_{dG,T}^2,
\end{aligned}
$$

$$
\begin{aligned}
\mathcal{I}_2 =& \sum_{F\in\mathcal{F}_I}\int_F\Big(\{\!\{\boldsymbol{\delta}_{\mathbf{u}}^{k-1}\}\!\}\cdot[\![T_h^k]\!]\Big)\,\{\!\{\delta_T^k\}\!\}-\frac{1}{2}\sum_{F\in\mathcal{F}}\int_F\Big|\{\!\{\boldsymbol{\delta}_{\mathbf{u}}^{k-1}\}\!\}\cdot\mathbf{n}\Big|\,[\![T_h^k]\!]\cdot[\![\delta_T^k]\!]\\
&+\frac{1}{2}\sum_{F\in\mathcal{F}_B}\int_F(\boldsymbol{\delta}_{\mathbf{u}}^{k-1}\cdot\mathbf{n})\,T_h^k\,\delta_T^k,\\
&\leq \sum_{F\in\mathcal{F}}\int_F|\{\!\{\boldsymbol{\delta}_{\mathbf{u}}^{k-1}\}\!\}|\,|[\![T_h^k]\!]|\frac{2|\{\!\{\delta_T^k\}\!\}|+|[\![\delta_T^k]\!]|}{2}\\
&\leq \sum_{F\in\mathcal{F}}h_\kappa^{1/2}\,\|\boldsymbol{\delta}_{\mathbf{u}}^{k-1}\|_F\,h_\kappa^{-2/3}\,\|[\![T_h^k]\!]\|_{L^3(F)}\,h_\kappa^{1/6}\,\|\delta_T^k\|_{L^6(F)}\\
&\leq \left(\sum_{\kappa\in\mathcal{T}_h}h_\kappa\,\|\boldsymbol{\delta}_{\mathbf{u}}^{k-1}\|_{\partial\kappa}^2\right)^{1/2}\left(\sum_{F\in\mathcal{F}}h_\kappa^{-2}\,\|[\![T_h^k]\!]\|_{L^3(F)}^3\right)^{1/3}\left(\sum_{F\in\mathcal{F}}h_\kappa\,\|\delta_T^k\|_{L^6(\partial\kappa)}^6\right)^{1/6}\\
&\leq C_{\mathrm{tr}}^2\,\|\boldsymbol{\delta}_{\mathbf{u}}^{k-1}\|\left(\sum_{F\in\mathcal{F}}h_\kappa^{-2}\,\|[\![T_h^k]\!]\|_{L^3(F)}^3\right)^{1/3}\|\delta_T^k\|_{L^6}\\
&\leq \epsilon C_{\mathrm{tr}}^4\|T_h^k\|_{dG,3}^2\|\boldsymbol{\delta}_{\mathbf{u}}^{k-1}\|_{dG,\mathrm{div}}^2+\frac{C_p}{4\epsilon\,\theta_M}\|\delta_T^k\|_{dG,T}^2,
\end{aligned}
$$

$$
\begin{aligned}
\mathcal{I}_3 =& \frac{1}{2}\sum_{F\in\mathcal{F}_I}\int_F[\![\mathbf{e}_{\mathbf{u}}^{k-1}]\!]_n\,\{\!\{T_h^k\,\delta_T^k\}\!\}\\
&\leq \sum_{F\in\mathcal{F}}h_\kappa^{-1/2}\,\|[\![\boldsymbol{\delta}_{\mathbf{u}}^{k-1}]\!]_n\|_F\,h_\kappa^{1/3}\,\|T_h^k\|_{L^3(F)}\,h_\kappa^{1/6}\,\|\delta_T^k\|_{L^6(F)}\\
&\leq \left(\sum_{F\in\mathcal{F}}h_\kappa^{-1}\,\|[\![\boldsymbol{\delta}_{\mathbf{u}}^{k-1}]\!]_n\|_F^2\right)^{1/2}\left(\sum_{F\in\mathcal{F}}h_\kappa\,\|T_h^k\|_{L^3(\partial\kappa)}^3\right)^{1/3}\left(\sum_{F\in\mathcal{F}}h_\kappa\,\|\delta_T^k\|_{L^6(\partial\kappa)}^6\right)^{1/6}\\
&\leq C_{\mathrm{tr}}^2\left(\sum_{F\in\mathcal{F}}h_\kappa^{-1}\,\|[\![\boldsymbol{\delta}_{\mathbf{u}}^{k-1}]\!]_n\|_F^2\right)^{1/2}\|T_h^k\|_{L^3}\,\|\delta_T^k\|_{L^6}\\
&\leq \epsilon C_{\mathrm{tr}}^4\|T_h^k\|_{dG,3}^2\|\boldsymbol{\delta}_{\mathbf{u}}^{k-1}\|_{dG,\mathrm{div}}^2+\frac{C_p}{4\epsilon\,\theta_M}\|\delta_T^k\|_{dG,T}^2
\end{aligned}
$$

By grouping all the results together, we obtain:

$$
\begin{aligned}
&\frac{\nu_m}{2k_M}\|\boldsymbol{\delta}_{\mathbf{u}}^k\|^2+\|\nabla_h\cdot\boldsymbol{\delta}_{\mathbf{u}}^k\|^2+\sum_{F\in\mathcal{F}_I}\|\sqrt{\xi}[\![\boldsymbol{\delta}_{\mathbf{u}}^k]\!]_n\|_F^2+\mathcal{D}_p(\delta_p^k,\delta_p^k)+\alpha_T\|\delta_T^k\|_{dG,T}^2\lesssim\\
&\frac{4k_M L_\nu^2}{\nu_m k_m^2}\|\mathbf{u}_h^k\|_{\tilde{\mathbf{L}}^\infty}^2\|\delta_T^{k-1}\|_{dG,T}^2+\frac{4k_M\beta^2}{\nu_m}\|\mathbf{u}_h^k\|_{\tilde{\mathbf{L}}^\infty}^2\|\boldsymbol{\delta}_{\mathbf{u}}^{k-1}\|^2\\
&+\epsilon\left(1+2C_{\mathrm{tr}}^4\right)\|T_h^k\|_{dG,3}^2\|\boldsymbol{\delta}_{\mathbf{u}}^{k-1}\|_{dG,\mathrm{div}}^2+\frac{5\,C_p}{4\epsilon\,\theta_M}\|\delta_T^k\|_{dG,T}^2
\end{aligned}
$$

we set $\epsilon = 5\,C_p/(2\theta_M\alpha_T)$ (cf. (4.1)) and we obtain:

$$\frac{\nu_m}{k_M}\|\boldsymbol{\delta}_{\mathbf{u}}^k\|_{dG,\mathrm{div}}^2 + \alpha_T\|\delta_T^k\|_{dG,T}^2 \lesssim \frac{k_M L_\nu^2}{\nu_m k_m^2}\|\mathbf{u}_h^k\|_{\mathbf{L}^\infty}^2\|\delta_T^{k-1}\|_{dG,T}^2 + \max\left(\frac{k_M\beta^2}{\nu_m}\|\mathbf{u}_h^k\|_{\mathbf{L}^\infty}^2,\ \frac{1}{\theta_M\,\alpha_T}\|T_h^k\|_{dG,3}^2\right)\|\boldsymbol{\delta}_{\mathbf{u}}^{k-1}\|_{dG,\mathrm{div}}^2.$$

Given (19), we infer that the map $(\boldsymbol{\delta}_{\mathbf{u}}^{k-1}, \delta_p^{k-1}, \delta_T^{k-1}) \to (\boldsymbol{\delta}_{\mathbf{u}}^k, \delta_p^k, \delta_T^k)$ is a contraction. Then, by applying the Banach fixed-point theorem the proof is concluded. □

5 Numerical results

This section assesses the performance of the proposed scheme in terms of accuracy and demonstrates its application to physically relevant test cases. All computations are performed in `FEniCS`. Convergence tests are carried out for both the dG–dG–dG and RT–dG–dG schemes, while physically relevant test cases use only the RT–dG–dG scheme. The two- and three-dimensional meshes consist of triangles and tetrahedra, respectively. The penalty coefficients α_1, α_2, and α_3 in (6) are set equal to 10. We denote by ℓ the polynomial degree for the temperature field and by m the degree for the pressure field. For the velocity field, ℓ is used in the dG–dG–dG scheme and m in the RT–dG–dG scheme, with $m = \ell - 1$ in all tests. With this choice, we expect the same accuracy in the L^2-norm for the pressure and in the energy norms for the velocity and temperature fields. In addition, the dG–dG–dG scheme gains one order of accuracy in the L^2-norm for the velocity field.

5.1 Convergence test case in two-dimensions

We set $\Omega = (0,1)^2$ with the following manufactured analytical solution:

$$\begin{aligned}\mathbf{u}(x,y) &= \begin{pmatrix} x^2\sin(2\pi y) \\ \dfrac{x}{\pi}\cos(2\pi y)\end{pmatrix},\ p(x,y) = (x^2 + 3y - 2xy)\sin(2\pi x),\\ T(x,y) &= (-y^2 + 2x)\cos(2\pi x);\end{aligned}$$

the boundary conditions and forcing terms are set accordingly. The model coefficients are reported in Table 2. We test the convergence of the dG-dG-dG scheme with respect to both the mesh size h and

$\mathbf{K}$ [m^2]	$\mathbf{I}$	β [Pa s^2/m^3]	1	$\boldsymbol{\Theta}$ [m^2/s]	$\mathbf{I}$

Table 2: Convergence tests of Section 5.1 and Section 5.2: model parameters

the polynomial degrees ℓ, m. The convergence of the RT-dG-dG scheme is tested only with respect to the mesh size h. For the h-convergence, we consider a sequence of successively fined triangular meshes and we set $\ell = 2$ and $m = 1$. For the p-convergence, we fix a mesh made of $N = 64$ triangular elements and we vary the polynomial degrees $\ell = [2,3,4,5,6]$, $m = [1,2,3,4,5]$. For what concerns the fixed-point iterative algorithm, a tolerance of 10^{-8} on the relative difference between two successive iterations is set. In Figure 1 we show the computed errors versus the mesh-size h (loglog scale).

We observe that the L^2-error for the pressure field and the energy-errors for the velocity and temperature fields decrease as h^2 for both the schemes. Moreover, as in both the methods the temperature equation is discretized with the use of dG method, we see that the L^2-error for the temperature field decays as h^3. The only difference we can clearly observe between the two schemes is in the L^2- error of the velocity field; indeed, in the dG-dG-dG scheme it decreases as h^3, while in the RT-dG-dG scheme it decreases as h^2. Thus, we gain one order of accuracy when using a full-dG discretization. We remark that by choosing $\ell = 2$, $m = 1$, we observe the same accuracy when looking at the energy-norm

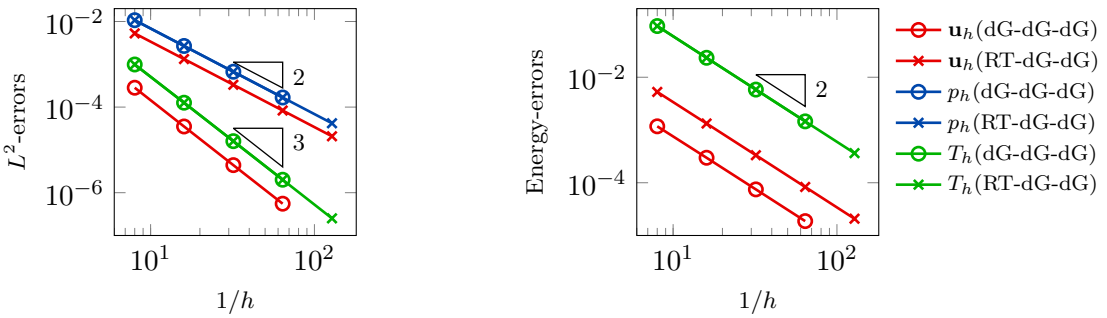

Figure 1: Test case of Section 5.1. Computed errors in L^2-norm (left) and energy-norms (right) versus $1/h$ (`log-log` scale).

of the velocity error, at the L^2-norm of the pressure error, and at the dG-norm of the temperature error. On average, 19 iterations of the fixed-point algorithm are required for achieving convergence of the dG-dG-dG algorithm and 14 for the RT-dG-dG one. It is worth noting that, apart from the velocity field errors all computed errors (in absolute value) are very similar.

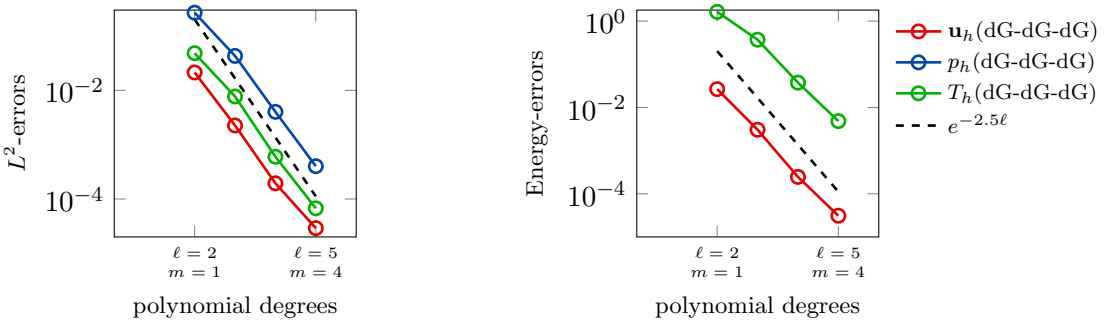

Figure 2: Test case of Section 5.1. Computed errors in L^2-norm (left) and energy-norms (right) versus the polynomial approximation degree ℓ (`semilog` scale).

For the dG-dG-dG scheme we also test the convergence with respect to the polynomial approximation degree. In Figure 2 we report the computed error versus the polynomial degree (semilog scale). We observe that the L^2-errors and energy-errors for all the three fields decay exponentially ℓ (and m, consequently).

5.2 Convergence test case in three-dimensions

In this section, we set $\Omega = (0,1)^3$, take the model coefficients as in Table 2, and consider boundary conditions and forcing terms inferred from the following manufactured solution:

$$\mathbf{u}(x,y,z) = \left(x^2\sin(2\pi y)\sin(2\pi z), -\frac{x}{\pi}\cos(2\pi y)\sin(2\pi x), \frac{2x}{\pi}\sin(2\pi y)\cos(2\pi z)\right)^T,$$
$$p(x,y,z) = (x^2 + 3y - 2xy + xz - z^2)\sin(2\pi x)\sin(2\pi y)\cos(2\pi z),$$
$$T(x,y,z) = (-3x + 2y^2 + 4yz + z)\cos(2\pi x)\cos(2\pi y)\sin(2\pi z).$$

We consider a sequence of successively refined tetrahedral meshes and set $\ell = 2$, $m = 1$. We have repeated the previous test case and reported in Figure 3 the computed errors versus $1/h$ (log-log scale). We observe that the convergence rates are as expected. In this set of simulations, the fixed-point iterative algorithm is stopped when the relative difference between two successive iterations is below 10^{-8}. On average, 17 iterations of the fixed-point algorithm are required for achieving convergence of the dG-dG-dG method, while 12 iterations are needed for the RT-dG-dG one.

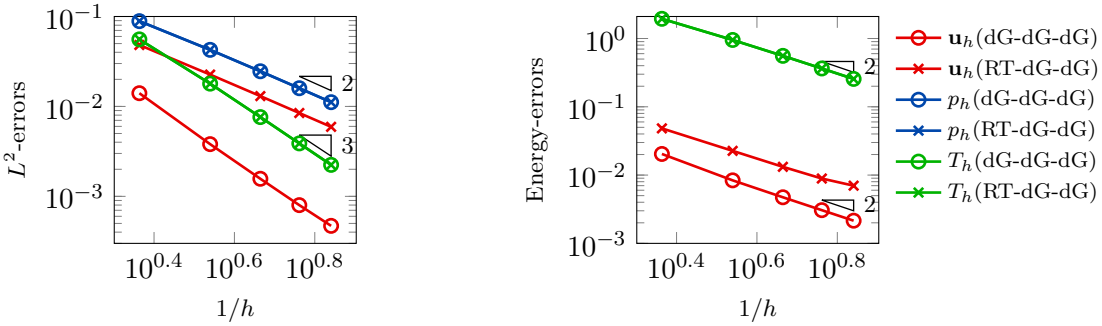

Figure 3: Test case of Section 5.2. Computed errors in L^2-norm (left) and energy-norms (right) versus $1/h$ (`log-log` scale).

5.3 Advection-dominated temperature transport in two-dimensions

In this section we propose a test case, inspired by [9], in which we investigate the transport of temperature by a flow that is governed by the DF law. We set $\Omega = (0,4)\times(0,2) \setminus (2,4)\times(0,1)$, with $\Gamma_{\text{in}} = 0\times(0,2)$ and $\Gamma_{\text{out}} = 4\times(1,2)$ and set the following boundary conditions:

$$\begin{cases} \mathbf{u}\cdot\mathbf{n} = u_{\text{in}} & \text{on } \Gamma_{\text{in}} \\ \mathbf{u}\cdot\mathbf{n} = u_{\text{out}} & \text{on } \Gamma_{\text{out}} \\ \mathbf{u}\cdot\mathbf{n} = 0 & \text{on } \partial\Omega\setminus(\Gamma_{\text{in}}\cup\Gamma_{\text{out}}) \\ T = T_{\text{in}} & \text{on } \Gamma_{\text{in}} \\ \boldsymbol{\Theta}\nabla T\cdot\mathbf{n} + \gamma(T - T_{\text{ext}}) = 0 & \text{on } \Omega\setminus\Gamma_{\text{in}}, \end{cases}$$

where $\gamma = 0.1$, $T_{\text{ext}} = 0.5$. The data u_{in}, u_{out}, and T_{in} takes the following general form

$$\phi(x) = \begin{cases} \phi_m, & \text{if } 0 \le x < a \\ \phi_m + \frac{\phi_M-\phi_m}{2}\left(1-\cos\left(\pi\frac{x-a}{b-a}\right)\right), & \text{if } a \le x < b \\ \phi_M, & \text{if } b \le x < c \\ \phi_m + \frac{\phi_M-\phi_m}{2}\left(1-\cos\left(\pi\frac{x-c}{d-c}\right)\right), & \text{if } c \le x < d \\ \phi_m, & \text{if } d \le x \le e, \end{cases}$$

with the following choice of parameters

$$\begin{cases} u_{\text{in}} = \phi(x) \text{ with } (a,b,c,d,e,\phi_m,\phi_M) = (0.5, 0.9, 1.1, 1.5, 2, 0, 1) \\ u_{\text{out}} = \phi(x) \text{ with } (a,b,c,d,e,\phi_m,\phi_M) = (1.25, 1.45, 1.55, 1.75, 2, 0, 1) \\ T_{\text{in}} = \phi(x) \text{ with } (a,b,c,d,e,\phi_{\min},\phi_{\max}) = (0.5, 0.9, 1.1, 1.5, 2, 0, 5) \end{cases}$$

As $\mathbf{f} = \mathbf{0}$ and $g = 0$, the displacement, pressure, and temperature fields are determined only by the boundary conditions. The computational domain is discretized via a computational mesh made of 4635 triangles with mesh size $h \sim 0.08$m and we set $\ell = 2$ for the temperature field and $m = \ell - 1 = 1$ for the velocity and pressure fields. We use the RT-dG-dG scheme for solving the problem. In Figure 4 (left) and Figure 4 (center), we show the results for the velocity and temperature fields, respectively. For clarity, velocity streamlines are superimposed on both fields. With the chosen boundary conditions, we mimic the injection of fluid in the central part of the inflow boundary Γ_{in} and the extraction of fluid in the central part of the outflow boundary Γ_{out}. The injected fluid is hotter than the reference temperature of the domain, and a Robin boundary condition is used to model heat exchange with the surrounding subsoil. In Figure 4 (left), the velocity field is shown; as expected, it is driven by the inflow and outflow boundary conditions. The streamlines clearly illustrate the flow behavior and highlight the point of high velocity at the recessed corner of the L-shaped domain. This behavior is consistent with expectations. Regarding the temperature field (Figure 4 (center)), we observe that, in this convection-dominated regime, the high temperature is transported by the fluid through the

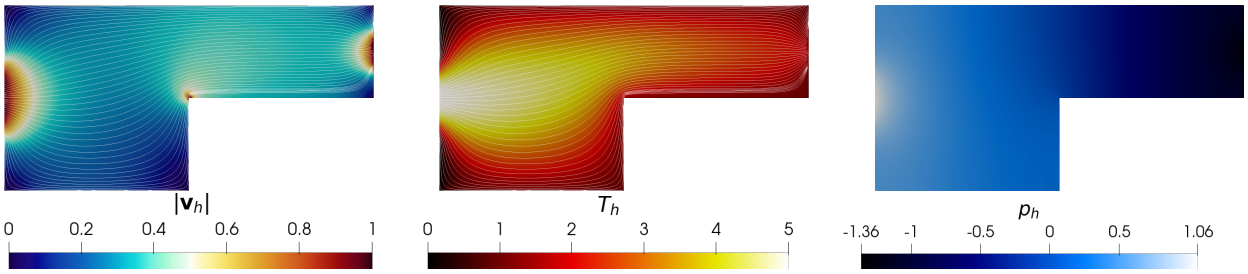

Figure 4: Test case of Section 5.3: computed velocity field (left), temperature field (center), and pressure field (right).

domain, and its distribution follows the flow lines. The temperature results also agree with what expected. Finally, in Figure 4(right), we display the pressure field. The pressure is higher in the fluid injection zone and then decreases in a manner resembling a linear drop toward the outflow boundary. To close the problem, we consider the pressure as an L^2 function with zero mean. Indeed, Figure 4 (right) shows that the computed pressure field satisfies the zero-mean condition.

5.4 Advection-dominated temperature transport in three-dimensions

In this section, we extend the test case presented in Section 5.3 to a three-dimensional setting. Then, we set $\Omega = (0,4)\times(0,2)\times(0,2) \setminus (2,4)\times(0,1)\times(0,1)$ and consider a set of boundary conditions that is similar to the two-dimensional case, where Γ_{in}, Γ_{out} are defined as $\Gamma_{\text{in}} = \{0\}\times(0,2)\times(0,2)$ and $\Gamma_{\text{out}} = \{4\}\times(0,2)\times(0,2) \setminus \{4\}\times(0,1)\times(0,1)$. The parameters of the functions u_{in}, u_{out} are taken as in Section 5.3 and they are considered constant along the z-direction. Moreover, as in the previous test case, we consider the forcing terms to be $\mathbf{f} = \mathbf{0}, g = 0$. The computational domain is discretized with a mesh consisting of 40544 tetrahedrons with mesh size $h \sim 0.25$m; moreover we set $\ell = 2$ for the temperature field and $m = \ell - 1 = 1$ for the velocity and pressure fields. The numerical results have been obtained based on employing the RT-dG-dG scheme. In Figure 5, we show the computed velocity field. Recall that this test case concerns convection-dominated temperature transport; thus a full understanding of the velocity field also provides insight into the temperature field. We observe that the results are consistent with those obtained in the two-dimensional setting, and, as expected, peaks in the velocity field occur at the inflow and outflow boundaries and along the edges surrounding the removed corner of the parallelepipedal domain. This is evident in both the slices that highlight the L-shaped part of the domain, cf. Figure 5 (top-right) and Figure 5 (bottom-right), but it is also evident by looking at the rectangular slices, cf. Figure 5 (top-left) and Figure 5 (bottom-left). In Figure 6 we show the results for the temperature field. As in the previous test case, we consider a convection-dominated pressure; then, as expected, in the behavior of the temperature field we clearly observe the convective phenomenon that predominates the diffusive one. We observe that, as in the two dimensional case, the temperature field follows the shape of the L-shaped domain (cf. Figure 6 (top-right)). In the correspondent rectangular part of the domain (cf. Figure 6 (bottom-right)) we still observe that shape of the field follows the L shape and there is no temperature diffusion in the bottom-left corner of the domain. When looking at the Figure 6 (top-left) and Figure 6 (bottom-left) slices we observe that also in this direction, the shape of the temperature follows an L-shaped pattern, coherent with the velocity field observed in Figure 5. In Figure 7 we display the pressure field. We observe that the pressure value is higher in the zone of the fluid injection and then decreases with a behavior similar to a linear decay towards the outflow boundary. We can observe from the slices Figure 7 (top-right), Figure 7 (bottom-right) that the part of the domain in which we observe the lowest value of pressure is the outflow boundary of the L-shaped part. In Figure 8 we give a volumetric representation of the three fields. In Figure 8 (left) it is possible to observe the behavior of the velocity field; we can observe that the fluid flows from the inflow boundary to the outflow one following the shape of the domain, with velocity peaks on the edges of the concave part of the domain, cf. Figure 5 too. In Figure 8 (center) we observe the behavior of the temperature field. By comparing Figure 8 (left) and Figure 8 (center) it is evident the convection-dominated nature of the test case, as the regions of high temperature of the fluid follow the flow pattern. In particular, we

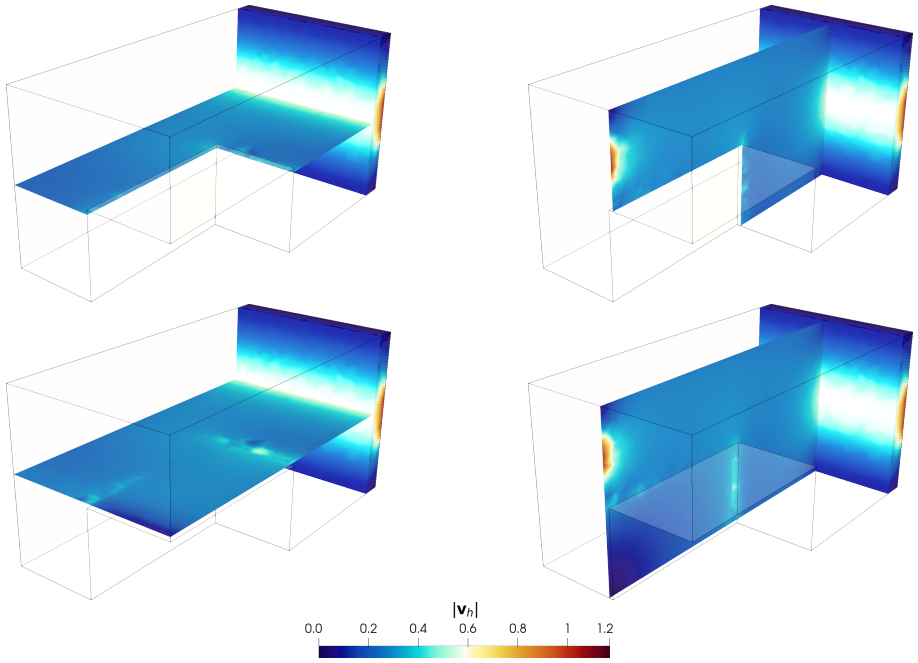

Figure 5: Test case of Section 5.4: computed velocity field. The domain is clipped at $x = 0.5$ and the four slices are at $y = 0.95$ (top-left), $y = 1.05$ (bottom-left), $z = 0.95$ (top-right), and $z = 1.05$ (bottom-right)

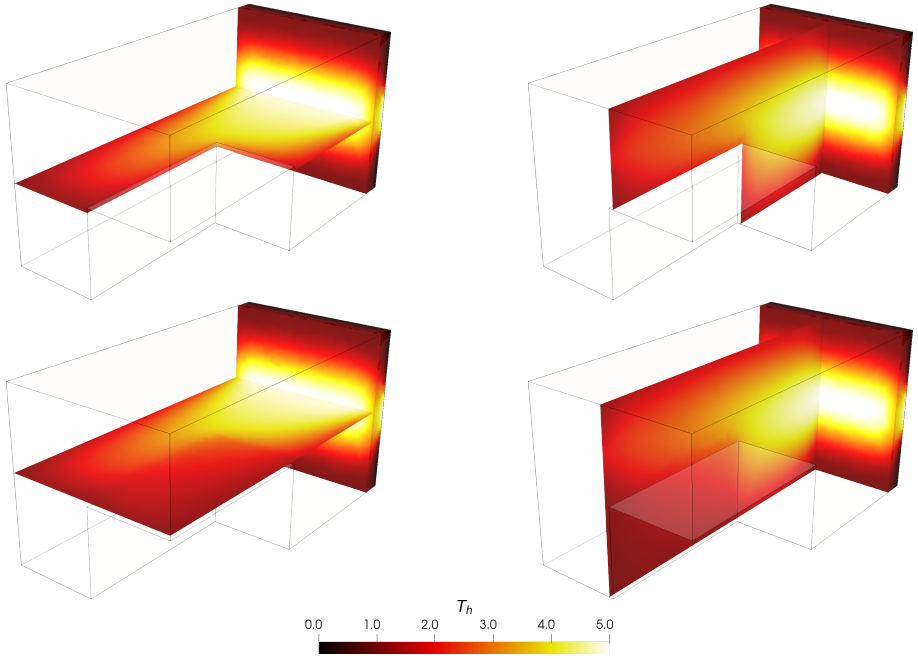

Figure 6: Test case of Section 5.4: computed temperature field. The domain is clipped at $x = 0.5$ and the four slices are at $y = 0.95$ (top-left), $y = 1.05$ (bottom-left), $z = 0.95$ (top-right), and $z = 1.05$ (bottom-right)

observe high-temperature regions in the inner corner of the domain.

6 Conclusions

In this work, we presented and analyzed in a unified framework two schemes for the numerical discretization of a DF fluid flow model coupled with an advection–diffusion equation describing the temperature distribution inside a fluid. The first approach relied on discontinuous discrete spaces for velocity, pressure, and temperature fields. In the second approach, the velocity was discretized in the RT space, with pressure and temperature remaining piecewise discontinuous. A fixed-point linearization strategy—naturally leading to a splitting solution approach—was employed to address

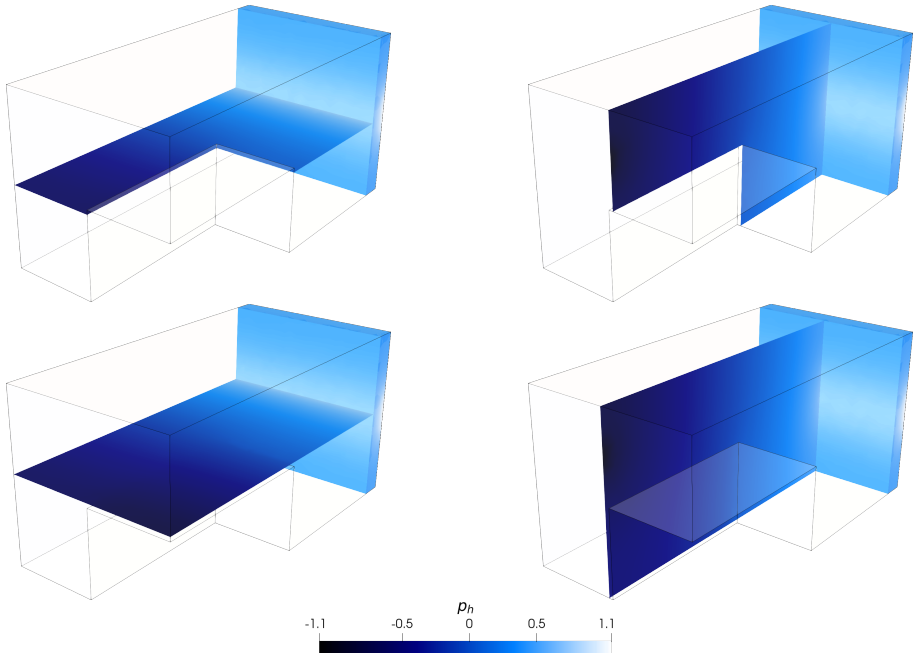

Figure 7: Test case of Section 5.4: computed pressure field. The domain is clipped at $x = 0.5$ and the four slices are at $y = 0.95$ (top-left), $y = 1.05$ (bottom-left), $z = 0.95$ (top-right), and $z = 1.05$ (bottom-right)

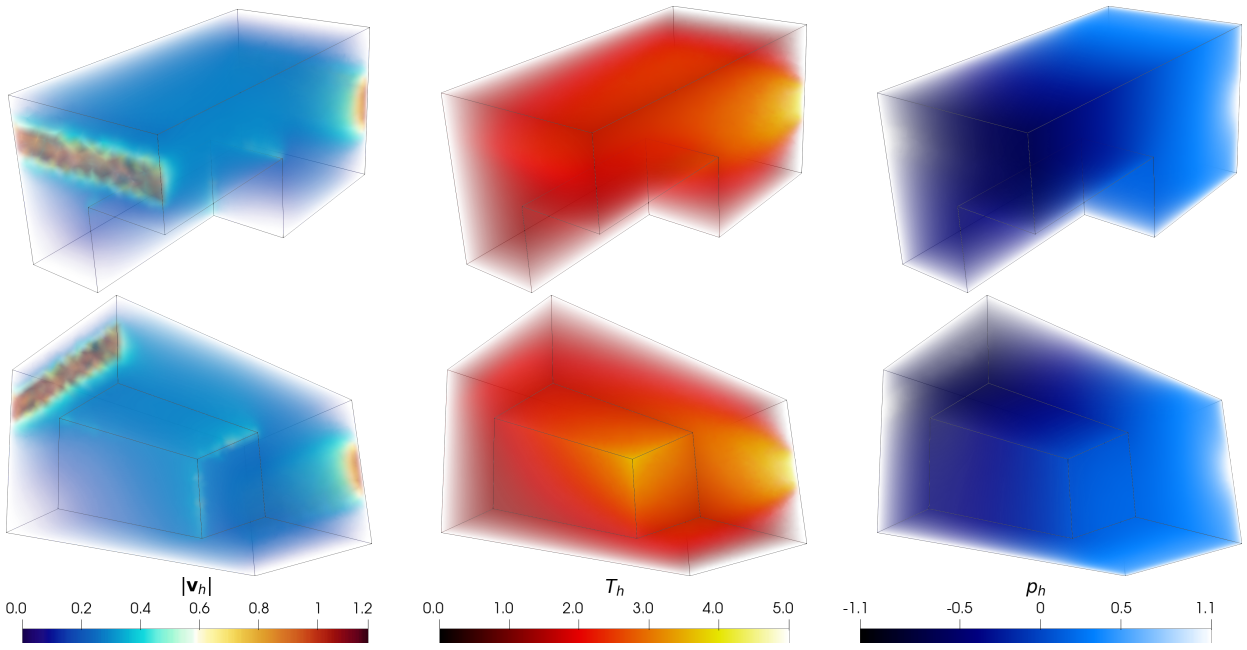

Figure 8: Test case of Section 5.4: volume representation of the temperature field (left), velocity field (center), and pressure field (right).

the nonlinearities. We carried out a unified stability analysis and established the convergence of the fixed-point algorithm under mild assumptions on the problem data. Extensive two- and three-dimensional numerical experiments confirmed the theoretical results and demonstrated the efficiency and robustness of the proposed schemes in physically relevant test cases. Future work could address the implementation of the dG-dG-dG scheme in the `lymph` software library [11] to fully exploit the advantages of this formulation and the flexibility offered by polytopal elements. Moreover, for computational efficiency in three-dimensional simulations, proper preconditioning techniques for the two subproblems have to be developed. Finally, we can include the DF law for the flow field in more sophisticated models, e.g., in the thermo-poroelasticity theory.

Acknowledgments

This work received funding from the European Union (ERC SyG, NEMESIS, project number 101115663). Views and opinions expressed are, however, those of the authors only and do not necessarily reflect those of the European Union or the European Research Council Executive Agency. Neither the European Union nor the granting authority can be held responsible for them. PFA, SB, and MB are members of INdAM-GNCS. The present research is part of the activities of "Dipartimento di Eccellenza 2023-2027", funded by MUR, Italy.

References

[1] R. Agroum, S. M. Aouadi, C. Bernardi, and J. Satouri. Spectral discretization of the Navier-Stokes equations coupled with the heat equation. *ESAIM: Math. Model. Numer. Anal.*, 49(3): 621–639, 2015.

[2] R. Agroum, C. Bernardi, and J. Satouri. Spectral discretization of the time-dependent Navier–Stokes problem coupled with the heat equation. *Appl. Math. Comput.*, 268:59–82, 2015.

[3] A. Allendes, G. Campaña, and E. Otárola. Numerical discretization of a Darcy-Forchheimer problem coupled with a singular heat equation. *SIAM J. Sci. Comput.*, 45(5):A2755–A2780, 2023.

[4] P. F. Antonietti, S. Giani, and P. Houston. *hp*-version composite discontinuous Galerkin methods for elliptic problems on complicated domains. *SIAM J. Sci. Comput.*, 35(3):A1417–A1439, 2013.

[5] P. F. Antonietti, C. Facciolà, A. Russo, and M. Verani. Discontinuous Galerkin approximation of flows in fractured porous media on polytopic grids. *SIAM J. Sci. Comput.*, 41(1):A109–A138, 2019.

[6] P. F. Antonietti, M. Botti, I. Mazzieri, and S. Nati Poltri. A high-order discontinuous Galerkin method for the poro-elasto-acoustic problem on polygonal and polyhedral grids. *SIAM J. Sci. Comput.*, 44(1):B1–B28, 2021.

[7] P. F. Antonietti, C. Facciolà, P. Houston, I. Mazzieri, G. Pennesi, and M. Verani. *High–order Discontinuous Galerkin Methods on Polyhedral Grids for Geophysical Applications: Seismic Wave Propagation and Fractured Reservoir Simulations*, pages 159–225. Springer International Publishing, Cham, 2021.

[8] P. F. Antonietti, L. Mascotto, M. Verani, and S. Zonca. Stability analysis of polytopic discontinuous Galerkin approximations of the Stokes problem with applications to fluid-structure interaction problems. *J. Sci. Comput.*, 90(1):23, 2021.

[9] P. F. Antonietti, G. Vacca, and M. Verani. Virtual element method for the Navier–Stokes equation coupled with the heat equation. *IMA J. Numer. Anal.*, 43(6):3396–3429, 2022.

[10] P. F. Antonietti, S. Bonetti, and M. Botti. Discontinuous Galerkin approximation of the fully coupled thermo-poroelastic problem. *SIAM J. Sci. Comput.*, 45(2):A621–A645, 2023.

[11] P. F. Antonietti, S. Bonetti, M. Botti, M. Corti, I. Fumagalli, and I. Mazzieri. lymph: discontinuous Polytopal Methods for Multi-Physics Differential Problems. *ACM Trans. Math. Softw.*, 51(1), 2025.

[12] D. N. Arnold. An interior penalty finite element method with discontinuous elements. *SIAM J. Numer. Anal.*, 19(4):742–760, 1982.

[13] D. N. Arnold, F. Brezzi, B. Cockburn, and L. D. Marini. Unified analysis of discontinuous Galerkin methods for elliptic problems. *SIAM J. Numer. Anal.*, 39(5):1749–1779, 2002.

[14] F. Bassi, L. Botti, A. Colombo, D. Di Pietro, and P. Tesini. On the flexibility of agglomeration based physical space discontinuous Galerkin discretizations. *J. Comput. Phys.*, 231(1):45–65, 2012.

[15] C. Bernardi, S. Maarouf, and D. Yakoubi. Spectral discretization of Darcy's equations coupled with the heat equation. *IMA J. Numer. Anal.*, 36(3):1193–1216, 10 2015.

[16] C. Bernardi, S. Dib, V. Girault, F. Hecht, F. Murat, and T. Sayah. Finite element methods for Darcy's problem coupled with the heat equation. *Numer. Math.*, 139(1):315–348, 2018.

[17] D. Boffi, F. Brezzi, M. Fortin, et al. *Mixed finite element methods and applications*, volume 44. Springer, 2013.

[18] S. Bonetti, M. Botti, I. Mazzieri, and P. F. Antonietti. Numerical modeling of wave propagation phenomena in thermo-poroelastic media via discontinuous Galerkin methods. *J. Comput. Phys.*, 489:112275, 2023.

[19] S. Bonetti, M. Botti, and P. F. Antonietti. Robust discontinuous Galerkin-based scheme for the fully-coupled nonlinear thermo-hydro-mechanical problem. *IMA J. Numer. Anal.*, 45(3): 1786–1820, 2024.

[20] M. Botti and L. Mascotto. Sobolev-Poincaré inequalities for piecewise $W^{1,p}$ functions over general polytopic meshes. *arXiv*, 2025.

[21] F. Brezzi and J. Douglas. Two families of mixed finite elements for second order elliptic problems. *Numer. Math.*, 47:217–235, 1985.

[22] A. Cangiani, E. H. Georgoulis, and P. Houston. *hp*-Version discontinuous Galerkin methods on polygonal and polyhedral meshes. *Math. Models Methods Appl. Sci.*, 24(10):2009–2041, 2014.

[23] A. Cangiani, Z. Dong, and E. H. Georgoulis. *hp*-version space-time discontinuous Galerkin methods for parabolic problems on prismatic meshes. *SIAM J. Sci. Comput.*, 39(4):A1251–A1279, 2017.

[24] A. Cangiani, Z. Dong, E. H. Georgoulis, and P. Houston. *hp-version discontinuous Galerkin methods on polytopic meshes*. SpringerBriefs in Mathematics. Springer International Publishing, 2017.

[25] O. Coussy. *Thermoporoelasticity*, chapter 4, pages 71–112. John Wiley & Sons, Ltd, 2003.

[26] J. Deteix, A. Jendoubi, and D. Yakoubi. A coupled prediction scheme for solving the Navier-Stokes and convection-diffusion equations. *SIAM J. Numer. Anal.*, 52(5):2415–2439, 2014.

[27] G. Deugoue, J. K. Djoko, V. S. Konlack, and M. Mbehou. Numerical analysis of a Darcy-Forchheimer model coupled with the heat equation. *J. Sci. Comput.*, 92(2):55, 2022.

[28] J. K. Djoko, V. S. Konlack, and M. Mbehou. Stokes equations under nonlinear slip boundary conditions coupled with the heat equation: a priori error analysis. *Numer. Methods Partial Differ. Equ.*, 36(1):86–117, 2020.

[29] A. Ern and J. Guermond. *Finite Elements II - Galerkin approximation, elliptic and mixed PDEs*. Springer Cham, 2021.

[30] J. Huang, Z. Yue, J. Zhang, K. Fu, and X. Feng. Numerical discretization of a Darcy–Forchheimer flow with variable density and heat transfer. *Comput. Appl. Math.*, 457:116252, 2025.

[31] R. Y. Jumah, A. Fawzi, and F. Abu-Al-Rub. Darcy-Forchheimer mixed convection heat and mass transfer in fluid saturated porous media. *Int. J. Numer. Methods Heat Fluid Flow*, 11(6): 600–618, 2001.

[32] J. C. Nedelec. Mixed finite elements in $\mathbb{R}^3$. *Numer. Math.*, 35(3):315–341, Sep 1980.

[33] H. Pan and H. Rui. Mixed element method for two-dimensional Darcy-Forchheimer model. *J. Sci. Comput.*, 52(3):563–587, 2012.

[34] P. A. Raviart and J. M. Thomas. A mixed finite element method for 2-nd order elliptic problems. In I. Galligani and E. Magenes, editors, *Mathematical Aspects of Finite Element Methods*, pages 292–315. Springer Berlin Heidelberg, 1977.

[35] H. Rui and H. Pan. A block-centered finite difference method for the Darcy-Forchheimer model. *SIAM J. Numer. Anal.*, 50(5):2612–2631, 2012.

[36] J. J. Salas, H. López, and B. Molina. An analysis of a mixed finite element method for a Darcy–Forchheimer model. *Math. Comput. Model.*, 57(9):2325–2338, 2013.

[37] T. Sayah, G. Semaan, and F. Triki. Finite element methods for the Darcy-Forchheimer problem coupled with the convection-diffusion-reaction problem. *ESAIM: Math. Model. Numer. Anal.*, 55 (6):2643–2678, 2021.

[38] J. M. Urquiza, D. N' Dri, A. Garon, and M. C. Delfour. A numerical study of primal mixed finite element approximations of Darcy equations. *Commun. Numer. Meth. En.*, 22(8):901–915, 2006.

[39] J. C. Ward. Turbulent flow in porous media. *J. Hydraul. Div.*, 90(5):1–12, 1964.

[40] M. F. Wheeler. An elliptic collocation-finite element method with interior penalties. *SIAM J. Numer. Anal.*, 15(1):152–161, 1978.

MOX Technical Reports, last issues

Dipartimento di Matematica
Politecnico di Milano, Via Bonardi 9 - 20133 Milano (Italy)

49/2025 Zanin, A.; Pagani, S.; Corti, M.; Crepaldi, V.; Di Fede, G.; Antonietti, P.F.; the ADNI
Predicting Alzheimer's Disease Progression from Sparse Multimodal Data by NeuralODE Models

48/2025 Temellini, E.; Ballarin, F.; Chacon Rebollo, T.; Perotto, S.
On the inf-sup condition for Hierarchical Model reduction of the Stokes problem

47/2025 Gimenez Zapiola, A.; Consolo, A.; Amaldi, E.; Vantini, S.
Penalised Optimal Soft Trees for Functional Data

46/2025 Mirabella, S.; David, E.; Antona, A.; Stanghellini, C.; Ferro, N.; Matteucci, M.; Heuvelink, E.; Perotto, S.
On the Impact of Light Spectrum on Lettuce Biophysics: A Dynamic Growth Model for Vertical Farming

45/2025 Caliò, G.; Ragazzi, F.; Popoli, A.; Cristofolini, A.; Valdettaro, L; De Falco, C.; Barbante, F.
Hierarchical Multiscale Modeling of Positive Corona Discharges

44/2025 Brivio, S.; Fresca, S.; Manzoni, A.
Handling geometrical variability in nonlinear reduced order modeling through Continuous Geometry-Aware DL-ROM

43/2025 Tomasetto, M.; Manzoni, A.; Braghin, F.
Real-time optimal control of high-dimensional parametrized systems by deep-learning based reduced order models

42/2025 Franco, N. R.; Manzoni, A.; Zunino, P.; Hesthaven, J. S.
Deep orthogonal decomposition: a continuously adaptive neural network approach to model order reduction of parametrized partial differential equations

41/2025 Torzoni, M.; Maisto, D.; Manzoni, A.; Donnarumma, F.; Pezzulo, G.; Corigliano, A.
Active digital twins via active inference

37/2025 Spreafico, M.; Ieva, F.; Fiocco, M.
Causal effect of chemotherapy received dose intensity on survival outcome: a retrospective study in osteosarcoma